# Effect of Helium Ion Irradiation on the Tunneling Behavior in Niobium/Aluminum/Aluminum Oxide/Niobium Josephson Junctions

by

Tiantian Zhang

A Thesis Presented in Partial Fulfillment
of the Requirements for the Degree
Master of Science

Approved June 2012 by the
Graduate Supervisory Committee:

Nathan Newman, Chair
John M. Rowell
Rakesh K. Singh
Ralph Chamberlin
Robert Wang

ARIZONA STATE UNIVERSITY

August 2012

ABSTRACT

The study of high energy particle irradiation effect on Josephson junction tri-layers is relevant to applications in space and radioactive environments. It also allows us to investigate the influence of defects and interfacial intermixing on the junction electrical characteristics.

In this work, we studied the influence of 2MeV Helium ion irradiation with doses up to $5.2 \times 10^{16}$ ions/cm$^2$ on the tunneling behavior of Nb/Al/AlOx/Nb Josephson junctions. Structural and analytical TEM characterization, combined with SRIM modeling, indicates that over 4nm of intermixing occurred at the interfaces. EDX analysis after irradiation, suggests that the Al and O compositions from the barrier are collectively distributed together over a few nanometers. Surprisingly, the IV characteristics were largely unchanged. The normal resistance, $R_n$, increased slightly (<20%) after the initial dose of $3.5\times10^{15}$ ions/cm$^2$ and remained constant after that. This suggests that tunnel barrier electrical properties were not affected much, despite the significant changes in the chemical distribution of the barrier's Al and O shown in SRIM modeling and TEM pictures. The onset of quasi-particle current, sum of energy gaps (2Δ), dropped systematically

from 2.8meV to 2.6meV with increasing dosage. Similarly, the temperature onset of the Josephson current dropped from 9.2K to 9.0K. This suggests that the order parameter at the barrier interface has decreased as a result of a reduced mean free path in the Al proximity layer and a reduction in the transition temperature of the Nb electrode near the barrier. The dependence of Josephson current on the magnetic field and temperature does not change significantly with irradiation, suggesting that intermixing into the Nb electrode is significantly less than the penetration depth.

ACKNOLEGEMENTS

This project would not have been possible without the help and support of numerous others. First I would like to express my greatest gratitude to my thesis advisor Professor Nathan Newman for his tremendous guidance, support and advice. Deepest gratitude is also due to Professor John M. Rowell for his invaluable suggestions and strong encouragement. Their role as excellent teachers and everlasting mentor helped me tackle the challenges and complete my thesis.

I would like to thank my committee members, Dr. Rakesh K. Singh, Professor Ralph Chamberlin and Professor Robert Wang for their time on the reading and criticism of my dissertation. Their comment and suggestions improved my work to a great degree.

I am grateful to Star Cryoelectronics LLC. for the device fabrication. And I would also like to show my gratitude to Dr. Ray Carpenter and Dr. John Mardinly for the TEM characterization. Their collaboration was extremely helpful for this project.

I would like to thank my colleagues in Newman research group for their help and assistance. Dr. Rakesh K. Singh gave me lots of insightful comments on my project and guidance on the particle irradiation study.

Dr. Lei Yu helped me with modeling calculations. Mr. Cameron Kopas helped me with many RBS irradiation experiment. Mr. Makram Abdelqader assisted me with many electrical measurements. Mr. Mengchu Huang shared with me some brilliant ideas and articles and also assisted in the work. I wish to thank all the other group members, Mr. Brett Strawbridge, Mr. Patrick Murray, Mr. Richard Hanley, Mr. Chris Traverse, Mr. Lingtao liu, Mr. Mahmoud Vahidi, Mr. Stephen Lehner, Mr. Nathan Cardinell, Mr. You Li, Mr. Dexuan Wang, Mr. Defeng Tao, for their valuable friendship and academic discussions.

I am also thankful to my friends at ASU, Pai Liu, Liuxian Zhang, Xiaofeng Wang, Chialing Fang, for their inspiration and friendship.

From my deep heart, I am grateful to my family for always been there for me.

TABLE OF CONTENTS

Page

Chapter Page

Chapter Page

LIST OF TABLES

LIST OF FIGURES

Figure Page

Figure Page

# CHAPTER 1 INTRODUCTION

Cooper pair tunneling in superconductor/insulator/superconductor structures (SIS) was first predicted by Brian D. Josephson [1] in 1962. It was subsequently observed by John M. Rowell and Phillip Anderson [2] in 1963. The application of the phenomenon, which now fall in a subset of devices called Josephson Junctions, has been used to produce practical devices and systems, including sensitive magnetometers SQUIDs [3], voltage standards [4], superconducting single-electron transistors [5], RSFQ digital logic circuits with frequency above 100 GHz [6], and microwave/IR detectors and mixers in astronomy and astrophysics [7].

In recent years, Josephson junctions have been widely used in applications where they are exposed to high energy particle irradiation, such as satellite-based devices and accelerator radiation detectors [8].

A number of experiments [8-11] have been reported on the effect of irradiation on the properties of tunnel devices. However, there is no published information available on the influence of irradiation on the

tunneling behavior, as a result of chemical changes near the barrier interface and in the proximity layer.

In this work we reviewed the physics of tunneling effect, characterized the properties of Josephson junctions, and presented experimental data and analysis of Nb/Al/$AlO_x$/Nb tunnel junctions exposed to high-energy alpha particle (Helium ion) irradiation. Our measurements used the common Nb/Al/AlOx/Nb Josephson junction configuration which was introduced in the 1980s [12], [13]. These devices have been found to be high quality, reliable and reproducible.

# CHAPTER 2 THEORY AND BACKGROUND

## 2.1 Superconductors

Superconductivity was discovered by H. Kamerlingh Onnes [14] on April 8, 1911 in Leiden. He found that resistance of superconductive material drops to zero when it is cooled below its critical temperature $T_c$. So far, Materials of many kinds, such as metals, alloys, ceramic materials, and organic compounds, have been found to have superconductivity. The value of critical temperature varies from material to material and ranges between <0.01K to 134K. The materials that have critical temperatures above 77K (boiling point of liquid nitrogen) are called high-temperature superconductors.

In 1933, the German physicists Walther Meissner and Robert Ochsenfeld [15] found that magnetic field is expelled from superconducting material during its transition to superconductive state. Also this implies that superconductivity could be destroyed when the external magnetic field exceeds critical field value Hc. At different temperatures below Tc, the critical field could be obtained:

$$H_c(T) = H_c(0)[1 - (T/T_c)^2] \tag{2.1}$$

This effect was explained by Fritz and Heinz London brothers in 1935 [17]. They showed the relation of supercurrent density $\vec{J_s}$ with electric field $\vec{E}$ and magnetic field $\vec{H}$ by two equations

$$\vec{E} = \frac{\partial}{\partial t}\left(\Lambda \vec{J_s}\right) \tag{2.2}$$

$$\vec{H} = -c\ \mathrm{curl}\left(\Lambda \vec{J_s}\right) \tag{2.3}$$

where

$$\Lambda = \frac{4\pi\lambda^2}{c^2} = \frac{m}{n_s e^2} \tag{2.4}$$

is a phenomenological parameter, $n_s$ is the number density of superconducting electrons, $\lambda$ is penetration depth, which characterized the distance that a magnetic field could penetrate in superconductors. Temperature dependence of penetration depth is

$$\lambda(T) = \lambda(0)[1 - (T/T_c)^4]^{-1/2} \tag{2.5}$$

Combined with Maxwell equation curl $\vec{H} = 4\pi\vec{J}/c$, the London equations become

$$\nabla^2 \vec{H} = \frac{\vec{H}}{\lambda^2} \tag{2.6}$$

The London equation implies that the Meissner effect was a consequence of the minimization of the electromagnetic free energy carried by superconducting current.

Two types of superconductors are distinguished by their response to magnetic field. In type I superconductors, the transition between superconducting and normal state occurs sharply at critical field $H_c$, while type II superconductors [18] have two critical field, between which there is a mixed state, as shown in Figure 2.1. In mixed state, among large superconducting regions, there exist small circular regions which are in normal state and carry units of quantum of flux

$$\Phi_0 = \frac{hc}{2e} = 2.07 \times 10^{-7} G \cdot cm^2 \tag{2.7}$$

Most type I superconductors are pure metals, while type II superconductors are usually metallic compounds, ceramics and alloys. Type I superconductors generally have very low critical temperatures, while all high temperature superconductors are type II superconductors.

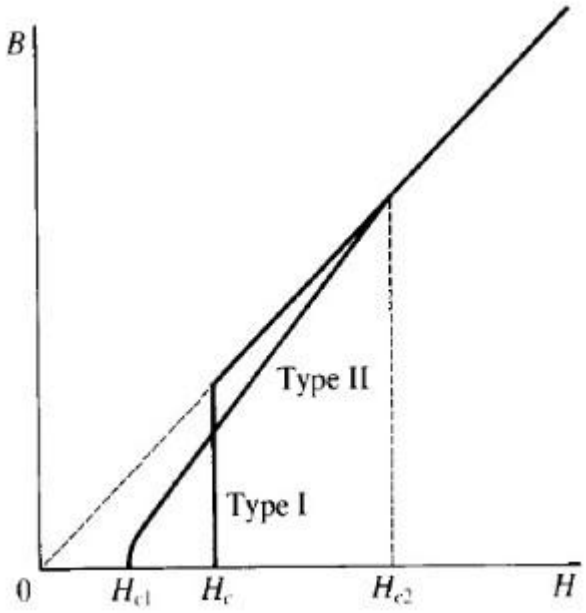


Figure 2.1 Type I and II superconductors. [19]

## 2.2 BCS Theory

In 1957, John Bardeen, Leon Cooper, and Robert Schrieffer [20] developed a microscopic theory of superconductivity, referred to as the BCS theory. The BCS theory successfully shows that electrons can be attracted to one another through interaction with the crystal lattice and be bound together in pairs, called Cooper pairs. Cooper showed that at low temperatures, electrons near the Fermi surface are unstable against the formation of bound pairs. The bound pairs could lead to an

energy gap $\Delta$ between ground state and excited state. The energy gap caused by Cooper pairs is given by [19]

$$\Delta = 2\hbar\omega_D e^{-2/N(0)V} \tag{2.8}$$

where $\omega_D$ is the Debye frequency, V is the attractive interaction energy, and N(0) is the density of states at the Fermi level for electrons of one spin orientation. With the formation of Cooper pairs, a new BCS ground state shows up instead of the normal ground state, as shown in Figure 2.2. The energy gap ($E_g$=$\Delta$) could be viewed as a barrier from ground state to electron excitation. The expression for the density of states in superconductors is [21]

$$N(E) = N(0)\frac{E}{\sqrt{E^2 - \Delta^2}} \qquad |E| \geq \Delta$$
$$N(E) = 0 \qquad |E| < \Delta \tag{2.9}$$

The dimension of Copper pair is called the coherence length, which is given by

$$\xi_0 = \frac{2\hbar\upsilon_F}{\pi E_g} \tag{2.10}$$

where $\upsilon_F$ is the electron velocity at the Fermi surface. The order of coherence length is 1μm.

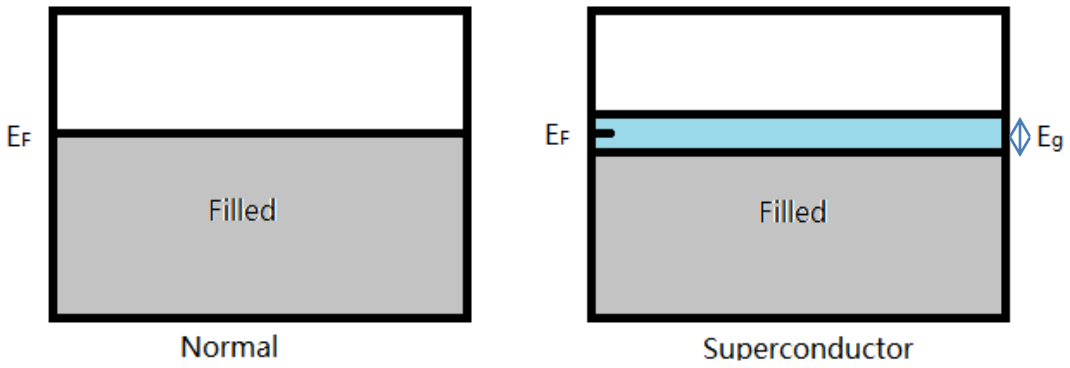


(a) (b)

Figure 2.2 (a), Conduction band in the normal state; (b), energy gap at the Fermi level in the BCS ground state. Electrons in excited states above the gap behave as normal electrons in rf fields: they cause resistance; at dc they are shorted out by the superconducting electrons. At absolute zero there are no electrons above the gap. [22]

## 2.3 Tunneling Effect

Tunneling is a process in which particles can travel from one conducting material to another through a narrow vacuum or a thin insulating material. In the view of classical physics it cannot happen. However, as a result of wave-particle duality of matter, the particle wave exponentially decays with the distance after it travel outside the conducting material, which means there is a chance for a particle to exist in the insulating barrier and on the other side of it. The tunnel current has the following expression [19]:

$$I = A|T|^2 \int_{-\infty}^{\infty} N_1(E)N_2(E + eV)[f(E) - f(E + eV)]dE \qquad (2.11)$$

where V it the applied voltage, eV is the resulting difference in the chemical potential across the junction, and N(E) is the conductor densities of states on the left and right side in tunnel junction. Tunneling between two normal metals (NIN), between a superconductor and a normal metal (SIN) and between two superconductors (SIS) will be explained below.

### 2.3.1 NIN (Normal metal–Insulator–Normal metal) Tunneling

In a NIN junction at 0K, all the electron states below Fermi level are filled, while all the state above are vacant, as shown in Figure 2.3(b). As a result of energy conservation, electrons fill the available state from the bottom to the higher energy level. And as a result of the Pauli exclusion principal, electrons tunnel to a filled state from one metal to a vacant state in the other. No electrons could tunnel in the condition shown in Figure 2.3(b) because there is no vacant state available. When a voltage is applied on the junction, the Fermi level of one metal is lifted up, and electrons could tunnel through the junction, as shown in Figure 2.3(c). The tunnel current is linearly dependent on the applied voltage, as shown in Figure 2.3(d), and (2.11) becomes

$$I_{nn} = A|T|^2 N_1(0) N_2(0) eV \equiv G_{nn} V \qquad (2.12)$$

where $G_{nn}$ is the tunneling conductance.

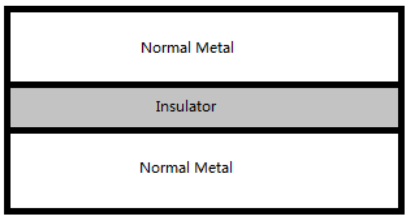


(a)

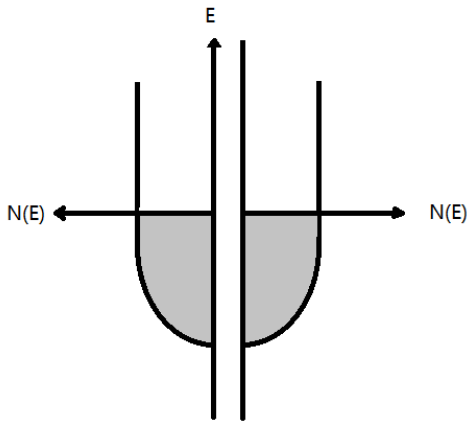


(b)

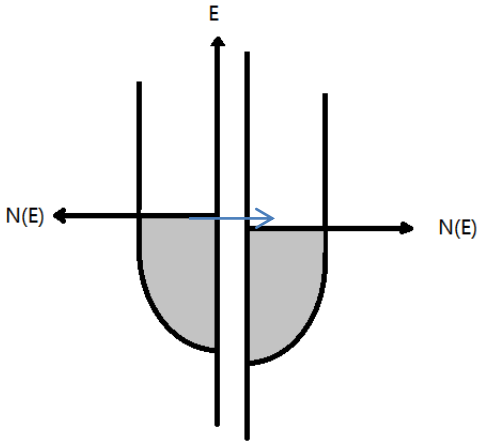


(c)

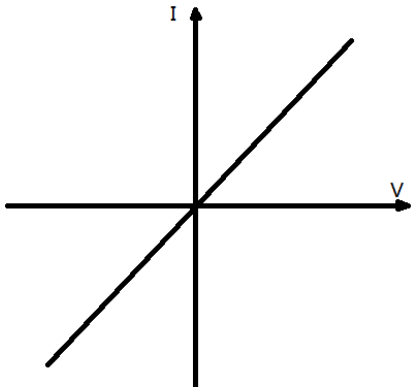


(d)

Figure 2.3 NIN tunneling. (a) NIN junction structure; (b) band diagram with no bias; (c) band diagram with bias; (d) IV characteristic.

### 2.3.2 SIN (Superconductor–Insulator–Normal metal) Tunneling

There is an energy gap (Δ) in superconductor, which corresponds to the energy necessary to break a Cooper pair. In a SIN junction at 0K at zero bias, electrons cannot tunnel from the superconductor to normal metal because all states are filled, and no electron tunnels from superconductor to normal metal because electron states at the same energy level are either filled or forbidden, as shown in Figure 2.4(b). When a voltage is applied, the Fermi level of superconductor is lifted up, and electrons could tunnel through the junction if the voltage is larger than Δ, as shown in Figure 2.4(c). The tunnel current is zero when applied voltage is smaller than Δ, and becomes linearly dependent on

the applied voltage as voltage increases, as shown in Figure 2.4(d), and (2.11) becomes

$$I_{ns} = \frac{G_{nn}}{e}\int_{-\infty}^{\infty}\frac{N_{2s}(E)}{N_2(0)}[f(E) - f(E + eV)]dE \qquad (2.13)$$

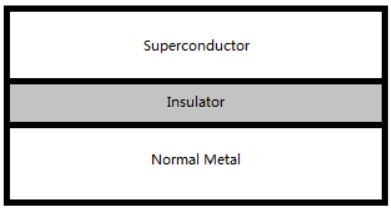


(a)

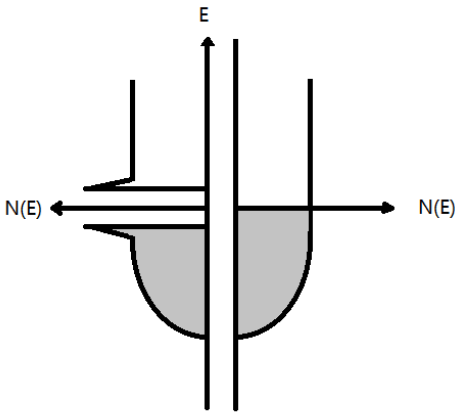


(b)

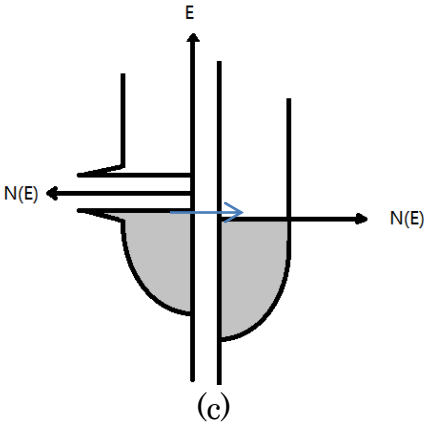


(c)

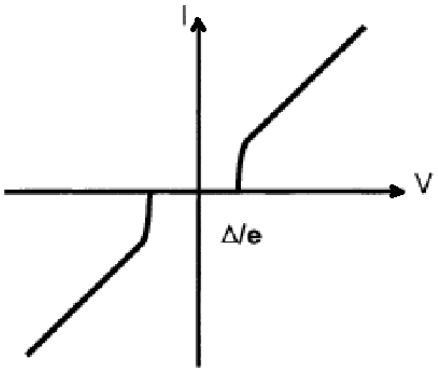


(d)

Figure 2.4 SIN tunneling. (a) SIN junction structure; (b) band diagram with no bias; (c) band diagram with bias; (d) IV characteristic.

### 2.3.3 SIS (Superconductor–Insulator–Superconductor) Tunneling

In a SIS junction at 0K, no single electron tunnels through the insulator until a voltage larger than 2Δ is applied on the junction, as shown in Figure 2.5(c). At zero voltage, current tunnels through a thin insulating barrier, which is caused by the paired electrons – Cooper pairs, shown as the vertical segment on y-axis in Figure 2.5(d). Expression (2.11) becomes

$$I_{ss} = \frac{G_{nn}}{e}\int_{-\infty}^{\infty}\frac{|E|}{|E^2-\Delta_1^2|^{1/2}}\frac{|E+eV|}{[(E+eV)^2-\Delta_2^2]^{1/2}}[f(E)-f(E+eV)]dE \quad (2.14)$$

In the IV curve of Josephson junctions, $I_c$ (critical current) is the current lying on the voltage axis, which is also called zero-voltage current. Gap voltage (2Δ) is the voltage value at which there is an immediate increase from 0 to 2Δ, which is different in various

superconducting materials. Δ of Niobium is 1.4meV. Normal resistance ($R_n$) is the resistance at the region larger than gap voltage, as indicated in Figure 2.5(d). It shows the properties of tunnel barrier. Dirtier barrier leads to higher $R_n$. Tunneling occurs in typical junctions only when the barrier is less than 2nm thick [23].

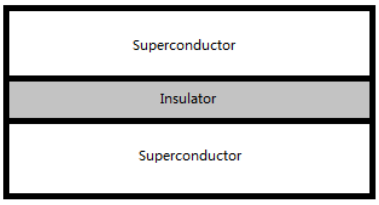


(a)

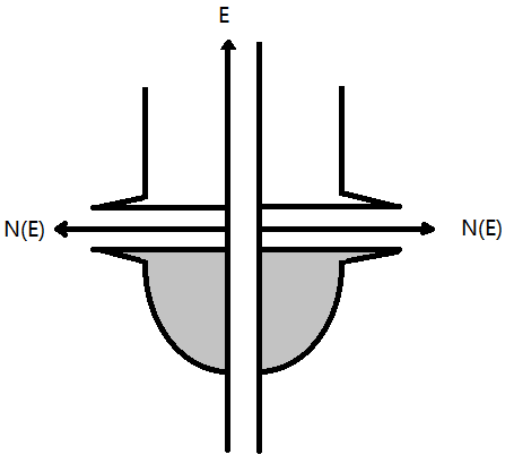


(b)

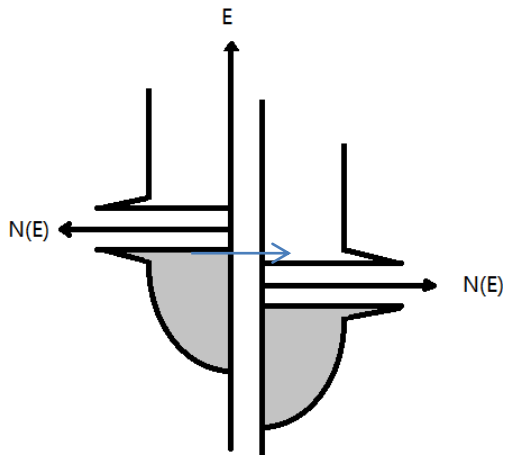


(c)

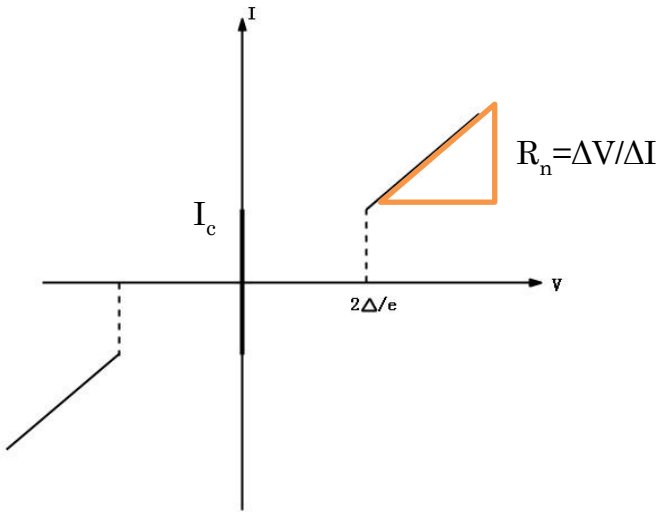


(d)

Figure 2.5 SIS tunneling. (a) SIS junction structure; (b) band diagram with no bias; (c) band diagram with bias; (d) IV characteristic.

## 2.4 Proximity Effect

A superconductor can induce superconducting properties into a normal metal coupled to it due to the proximity effect. At an N-S interface,

some electron pairs leak into the normal metal while some quasi-particles leak into the superconductor, thereby reducing the transition temperature of the superconductor [24].

The theory to explain this phenomenon is called Andreev reflection [25]. On the interface from normal state material at energies less than superconducting energy gap, an incident electron (hole) forms a Cooper pair in the superconductor with the retroflection of a hole (electron) of opposite spin and momentum to incident electron (hole). Since the pair consists of two electrons with opposite spin, a second electron (hole) forms the pair in superconductor. In this N-S sandwich, both the density of states and the effective electron-electron interaction are varying parameters across the structure.

Based on the theory above, de Gennes [26] found that the coherence length, dimension of Cooper pairs, is

$$\xi_{N,S} = \left(\frac{\hbar D_{N,S}}{2\pi k_B T}\right)^{1/2} \tag{2.28}$$

where $D_{N,S} = \frac{1}{3}\upsilon_{F_{N,S}} l_{N,S}$ is the diffusion coefficient with the Fermi velocity $\upsilon_F$ and the electron mean free path $l_{N,S}$. In this theory, it is assumed that $l_{N,S} \ll \xi_{N,S}$ (dirty limit) and that the films are relatively

thick. The order parameter near the N-S interface is shown in Figure 2.6.

A bound state will form at the surface of materials with an energy gap in the bulk electron spectrum. At the superconductor surfaces, quasi-particles with energies inside the superconducting gap $\Delta$ may be trapped in bound states in quantum wells, which are formed by total reflection against the vacuum and total Andreev reflection against the superconductor. Since an electron reflects as a hole and sends a Cooper pair into superconductor, the surface states give rise to resonant transport of quasi-particle and Cooper pair currents, and may be observed in tunneling spectra. In superconducting junctions these surfaces may hybridize and form bound Andreev states, trapped between the superconducting electrodes. [27]

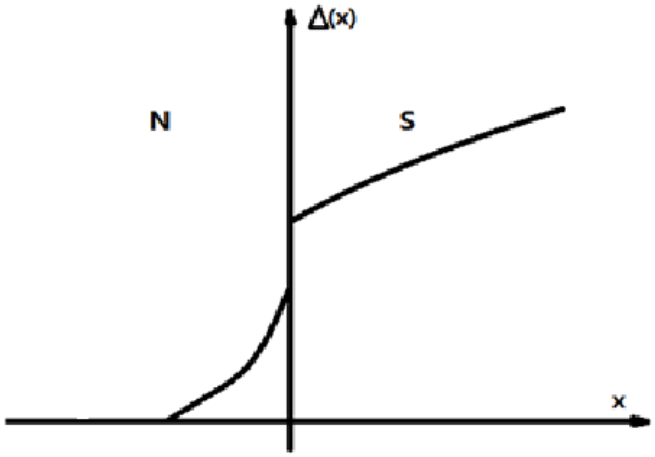


Figure 2.6 Order parameter at the N-S interface.

For a system of multiple layers in the dirty limit with different transition temperature, the theory of de Gennes and Werthamer [28] gives the proximity effect transition temperature for these systems. In conjunction with the boundary conditions, Broussard [29] developed the following expressions as the boundary condition effects on the Tc of proximity effect systems

$$\chi(\xi_i^2 k_s^2) = \ln\left(\frac{T_{cs}}{T_c}\right) \tag{2.15}$$

$$\chi(-\xi_i^2 k_s^2) = \ln\left(\frac{T_{cn}}{T_c}\right) \tag{2.16}$$

$$\frac{k_s}{k_n}\frac{\rho_n}{\rho_s}\tan\left(\frac{k_s d_s}{2}\right) = \tanh(k_n d_n) \tag{2.17}$$

where $\chi(x) = \psi\left(\frac{1}{2}+\frac{1}{2}x\right) - \psi(x)$ and the digamma function $\psi(x)$ can be expressed as $\psi(x) = \frac{1}{\Gamma(x)}\left(\frac{d\Gamma(x)}{dx}\right)$, $\xi_i$ is the coherence length of the superconductor, $T_{cs}$ is the $T_c$ of superconductor, $T_{cn}$ is the $T_c$ of normal

metal, $D_s$ is the thickness of the superconductor, $D_n$ is the thickness of the normal layer, $\rho_s$ is the residual resistivity of the superconductor, $\rho_n$ is the resistivity of the metal.

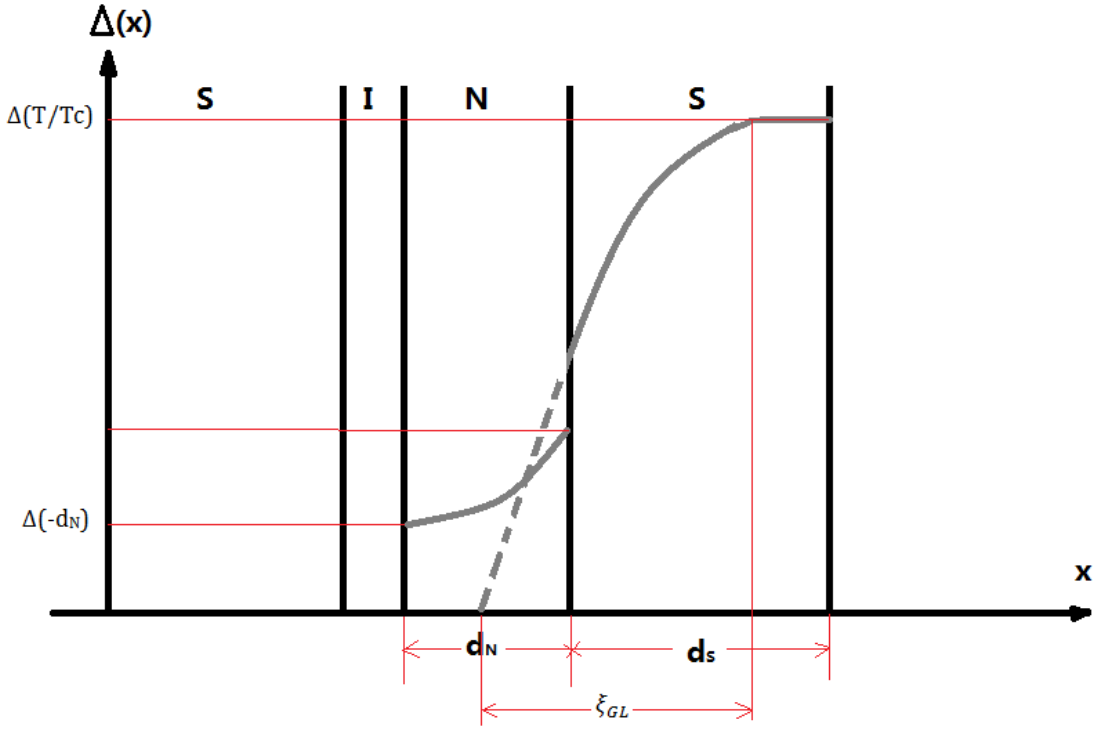


Figure 2.7 Order parameter in S-I-N-S junction. [29]

In superconductor-insulator-normal metal-superconductor (S-I-N-S) sandwich junctions, the coupling of the pair wave function in the superconductor S with that in the proximized sandwich N-S is realized through a dielectric barrier, as shown in Figure 2.7.

It's assumed that the order parameter in the right superconductor layer is decribed by the linear Ginzburg-Landau equation

$$\Delta = \Delta_0 \left(\frac{T}{T_c}\right) \sin \pi \left(\frac{x+b}{2\xi_{GL}}\right) \tag{2.29}$$

within the region near N-S interface, and by the B.C.S. theory

$$\Delta = \Delta_0 \left(\frac{T}{T_c}\right) \tag{2.30}$$

within the region far from N-S interface. And the order parameter in normal metal is same as discussed in Figure 2.6.

## 2.5 Josephson Junctions

The Josephson Effect is when supercurrent flows between two superconductors separated by a thin insulating barrier (i.e. SIS), non-superconducting metal (i.e. SNS) or a narrow restriction (i.e. Dayem Bridge). This arrangement is known as a Josephson junction. The zero-voltage current is called Josephson current, or Cooper pair current. In this project, Nb/Al/AlOx/Nb Josephson junction was studied.

### 2.5.1 Josephson Equations

If the separation between the two superconductors is large, the pairs can be described as the following wave function [21]

$$j\hbar \frac{\partial |\psi\rangle}{\partial t} = \mathcal{H} |\psi\rangle \tag{2.15}$$

If the separation is small, there is an interaction between two superconductors. Considering the projections on the two base states, (2.15) becomes

$$j\hbar\frac{\partial\psi_R}{\partial t} = E_R\psi_R + K\psi_L$$
$$j\hbar\frac{\partial\psi_L}{\partial t} = E_L\psi_L + K\psi_R \qquad (2.16)$$

where L and R means the left and right side. Considering a voltage V across the junction, the energy difference would be $E_L - E_R = 2eV$, so that

$$j\hbar\frac{\partial\psi_R}{\partial t} = -eV\psi_R + K\psi_L$$
$$j\hbar\frac{\partial\psi_L}{\partial t} = eV\psi_L + K\psi_R \qquad (2.17)$$

Substituting the expressions for wave function

$$\psi_L = \rho_L^{1/2}e^{j\varphi L}$$

$$\psi_R = \rho_R^{1/2}e^{j\varphi R}$$

and introducing the phase difference

$$\varphi = \varphi_L - \varphi_R$$

we get the following equations

$$\frac{\partial\rho_L}{\partial t} = \frac{2}{\hbar}K\sqrt{\rho_L\rho_R}\sin\varphi$$
$$\frac{\partial\rho_R}{\partial t} = -\frac{2}{\hbar}K\sqrt{\rho_L\rho_R}\sin\varphi$$
$$\frac{\partial\rho_L}{\partial t} = \frac{K}{\hbar}\sqrt{\rho_L/\rho_R}\cos\varphi + \frac{eV}{\hbar}$$

$$\frac{\partial \rho_R}{\partial t} = \frac{K}{\hbar}\sqrt{\rho_L/\rho_R}\cos\varphi - \frac{eV}{\hbar} \tag{2.18}$$

The Josephson current between two superconducting electrodes is

$$I = I_1 \sin\varphi \tag{2.19}$$

where $I_1$ is the maximum zero-voltage current that can be passed by the junction. The difference of phase across junction $\varphi$ would evolve according to

$$d\varphi/dt = 2eV/\hbar \tag{2.20}$$

Equation 2.19 and 2.20 are the constitutive relations of the Josephson effect.

### 2.5.2 Temperature dependence of critical current

The Josephson current is dependent on temperature. $I_1$ in equation (2.19), the maximum zero-voltage current, could be expressed by [21]

$$I_1(0) = \frac{\pi}{2}\frac{\hbar\Delta}{eR_n} \tag{2.21}$$

where $R_n$ is the normal resistance of the Josephson junction. This expression allows us to estimate the expected maximum value for d.c. Josephson current by looking at the IV characteristic of the junction.

In the case T>0, by applying the microscopic theory to a tunnel junction, Ambegaokar and Baratoff [31] showed that the temperature dependence of critical current is

$$I(T) = \frac{\pi}{2}\frac{\Delta(T)}{R_n}\tanh\left(\frac{\Delta(T)}{2k_B T}\right) \tag{2.22}$$

where $\Delta(T)$ is the energy gap at certain temperature, and has the following expression when T is close to $T_c$,

$$\Delta(T) = 1.74\Delta(0)\left[1 - \frac{T}{T_c}\right]^{1/2} \tag{2.23}$$

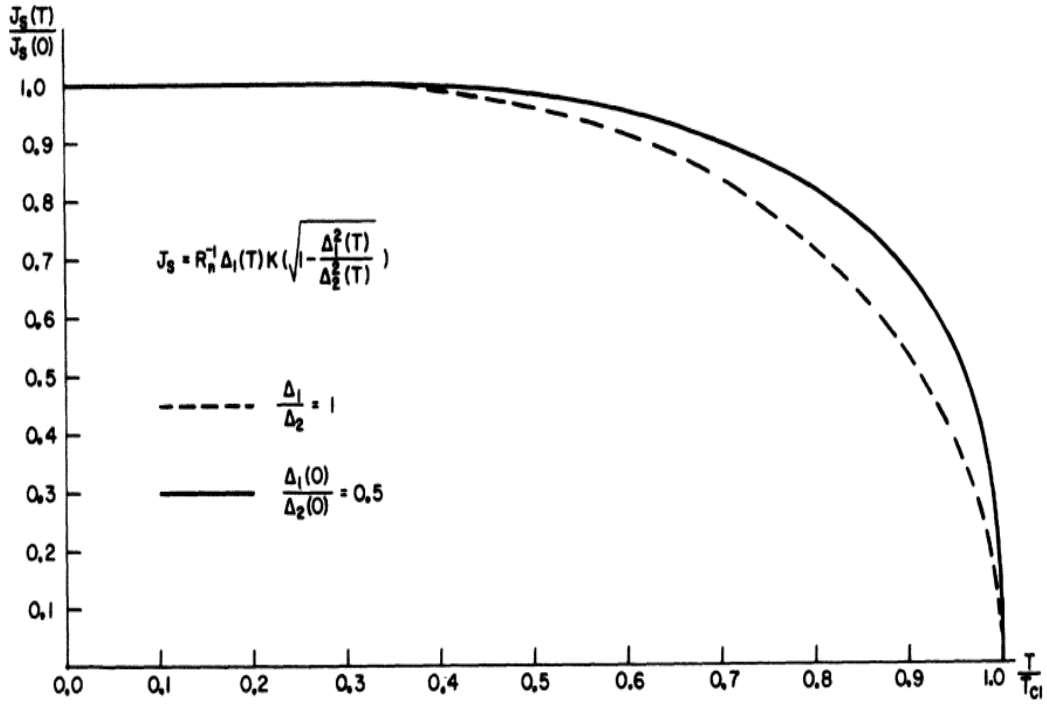


Figure 2.8 Theoretical temperature dependence of the maximum dc Josephson current. [31] In this project, the junctions have $\Delta_1 = \Delta_2$, so the dashed line applies.

### 2.5.3 Magnetic field dependence of critical current

A magnetic field perpendicular to the junction current could modulate the critical current. As shown in Figure 2.9(a), a magnetic field H

applied in the y direction, will cause a magnetic field inside the junction which is equal to [21]

$$\varphi(x) = \frac{2\pi d}{\Phi_0} H_y x + \varphi_0 \tag{2.23}$$

where $\Phi_0$ is the flux quantum as discussed in equation (2.7), and $\varphi_0$ is an integration constant. The current density on x direction, as shown in Figure 2.9(b), can be expressed by

$$J(x) = J_1 \sin\left(\frac{2\pi d}{\Phi_0} H_y x + \varphi_0\right) \tag{2.24}$$

where $J_1$ is the maximum current density. The total current in the junction can be obtained by integration

$$I_1(k) = \left| \int_{-\infty}^{+\infty} dx J(x) e^{jkx} \right| \tag{2.25}$$

where $k = \frac{2\pi d}{\Phi_0} H_y$.

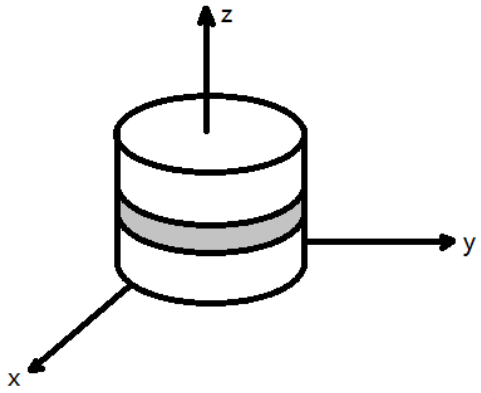


(a)

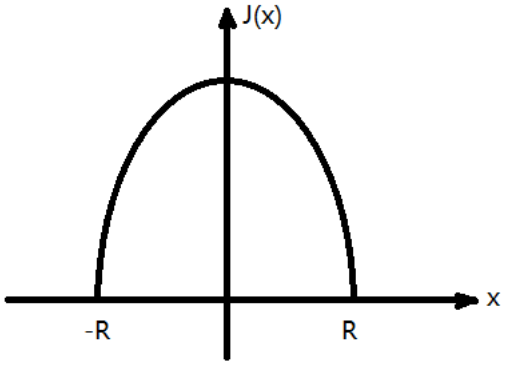


(b)

Figure 2.9 (a) Geometrical configuration of circular Josephson junction. (b) Current density J(x) distribution of circular Josephson junction.

In a circular geometry junction, the current density is given by

$$J(x) = \int_{-\sqrt{R^2-x^2}}^{\sqrt{R^2-x^2}} dy J_1 = 2J_1\sqrt{R^2 - x^2} \tag{2.26}$$

After integration, Matisoo [32] showed the magnetic field dependence of critical current is given by

$$I(k) = I_1 \left| \frac{\text{Bessel } J_1(kR)}{\frac{1}{2}(kR)} \right| \tag{2.27}$$

where $I_1 = \pi R^2 J_1$, and $J_1(x)$ is a Bessel function of the first kind.

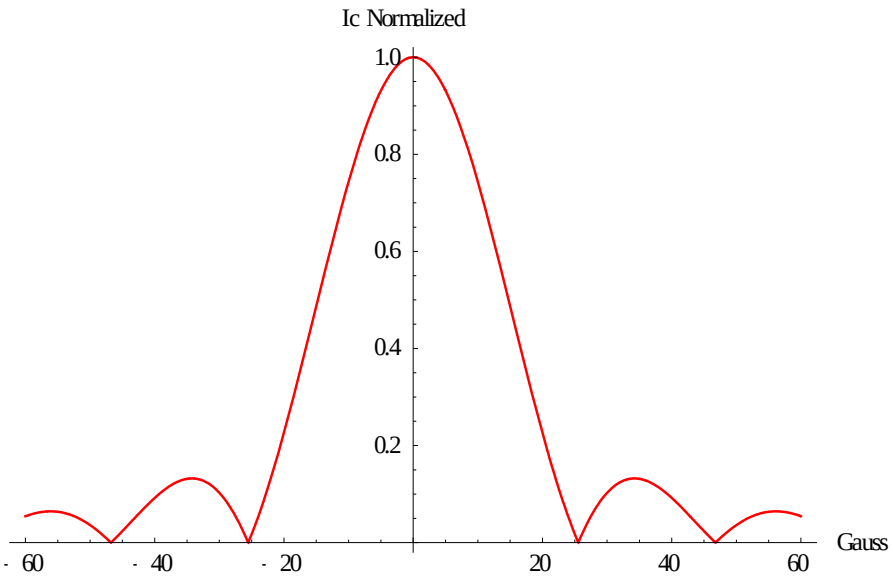


Figure 2.10 Theoretical magnetic field dependence of the maximum dc Josephson current for a circular junction.

## 2.6 High Energy Particles Irradiation

### 2.6.1 Source of irradiation

High energy particles, such as electrons alpha particles, protons, neutrons, photons, and quark, could be produced by radioactive and scattering process. There are two main kinds of radiation exposures: natural sources radiation and man-made sources radiation [33].

### 2.6.2 Effect of radiation

The sum of affects in a specific device is carried based on elemental composition, geometry, size, and many other factors, but the small scale physical interaction can generally be explained in several ways:

creating of point defects, intermixing between layers, and ionizing radiation effects. Devices can be affected by one, or all of these depending on the kind of radiation, the irradiation dose, and device properties [34].

The most common defect associated with radiation damage is point defects. When high energy particles are implanted, collision between the incident particle and the device lattices could break the bonds surrounding an atom and displace it from its lattice site. The displaced atom could hit another atom with sufficient energy to displace the second atom and so forth. If the device has multiple layers, intermixing may be caused at interface as a result of knock in and knock back of atoms. The created defects, if in sufficient concentration, can change the mechanical, structural, physical and/or electronic properties of materials.

### 2.6.3 Irradiation on Nb/Al/AlOx/Nb Josephson junctions

A number of papers [8-11] have reported studies on the high-energy particle irradiation on the properties of tunnel devices. However, there is not a strong fundamental understanding of how the changes in the

structural properties of the electrodes, barrier, and proximity layer influence the electrical properties.

In Ref [8], $Nb/Al_2O_3/Nb$ tunnel junctions were irradiated using a fluence of $7.6\times10^{14}$ protons/cm$^2$ at energy of 63 MeV. No significant changes in the IV characteristics were observed, as illustrated in Figure 2.11 (a). The before and after irradiation curves plotted on the graph are virtually identical, so only one is visible. The author concluded that no permanent damage occurred at this level of irradiation. To quantitatively access the changes in the structural properties for this experiment, a simulation using SRIM was performed on this structure. As shown in Figure 2.11 (b), the atom distribution change in the tri-layer junction is small, with vacancy and interstitial concentrations on the order of 1% and possibly less as a result of recombination of vacancy-interstitial defects. Later, we will show that higher levels of irradiation are needed before a significant change in the electrical properties is observed.

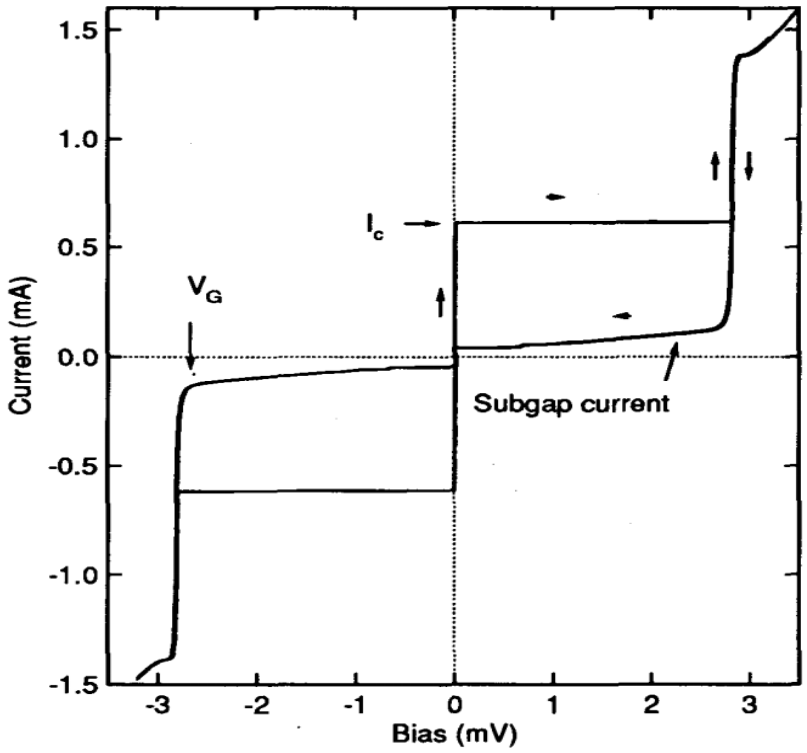


(a)

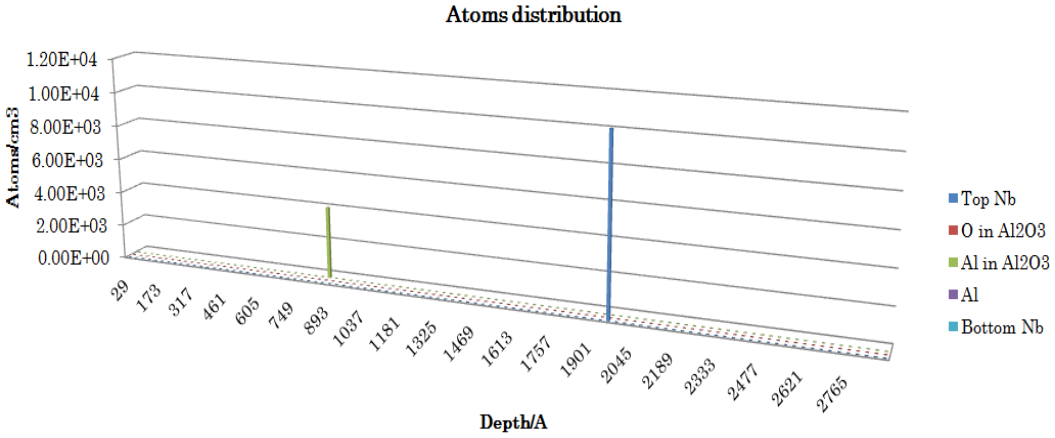


(b)

Figure 2.11 (a) IV curves from a Nb shift register measured both before and after irradiation with $7.6\times10^{14}$ protons/cm$^2$ at energy of 63MeV. The two curves measured at 4.2K are virtually identical. [8] (b) SRIM simulation of the same junction.

In Ref [9], as shown in Table 2.1 and Figure 2.12, a change in the tunneling behavior of Nb/Al/AlOx/Nb junctions was observed after exposure to a 10 MeV proton beam with a fluence of up to $1.3\times10^{11}$ /cm$^2$. The mechanism responsible for the changes in the electrical properties was not stated.

| Chip - Wafer | Calculated dose (protons/cm$^2$) | Experimental dose (protons/cm$^2$) | $\Delta V_{max} = V_{before} - V_{after}$ |
|---|---|---|---|
| 17 – S6I14I (8 junctions) | $2.8\ 10^9$ | $2.8\ 10^9$ | - 0.01 |
| 17 – S9I14I (10 junctions) | $2.8\ 10^9$ | $2.8\ 10^9$ | + 0.02 |
| 11 – S9I14I (10 junctions) | $2.8\ 10^{10}$ | $2.8\ 10^{10}$ | - 0.03 |
| 12 – S9I14I (10 junctions) | $2.8\ 10^{10}$ | $2.8\ 10^{10}$ | - 0.02 |
| 6 – S9I14I (8 junctions) | $1.1\ 10^{11}$ | $1.3\ 10^{11}$ | - 0.03 |
| 7 – S9I14I (10 junctions) | $1.1\ 10^{11}$ | $1.1\ 10^{11}$ | - 0.01 |
| 11 – S6I14I (8 junctions) | $2.8\ 10^9$ | Calibration problem | + 0.1 |

Table 2.1 Summary of energy gap change of Nb/Al/AlOx/Nb junctions irradiated by different level of dose with 10MeV energy protons. [9]

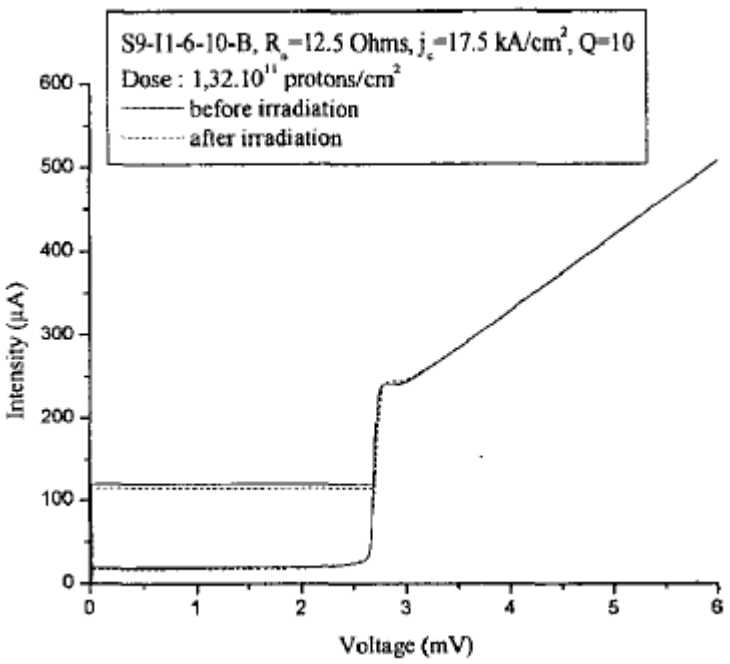


(b)

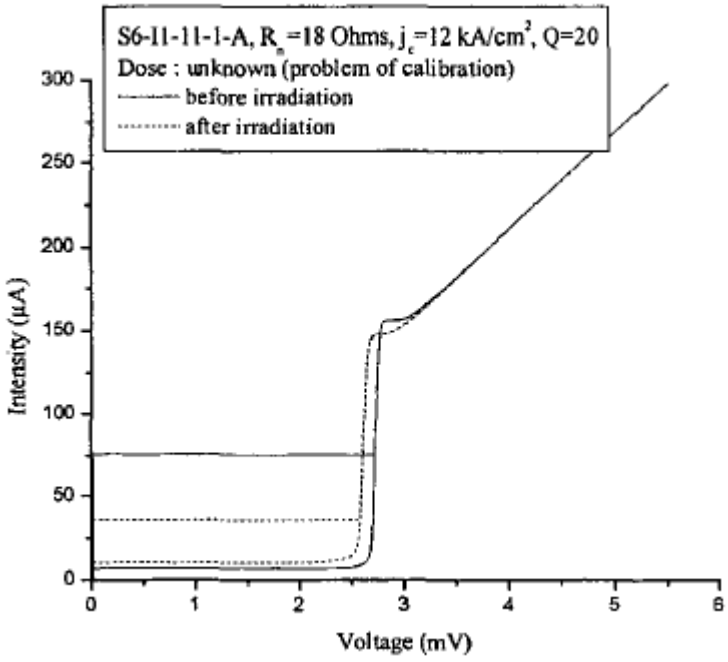


(c)

Figure 2.12 IV curves of Nb/Al/AlOx/Nb junctions before and after irradiation for different doses. [9]

In Ref [10], the authors investigated the effects of 6.5 MeV proton beam irradiation on Nb/AlOx/Nb junctions at a fluence of $10^{16}$ protons/cm$^2$. They state that there is not any measurable change in the electrical characteristics of the tunnel junctions from the irradiation. However, in the Figure 2.13 (a), the IV plot shows a shift in energy gap, and a slight change in resistance. The same samples were also irradiated by 235 MeV $Au^{16+}$ ions with a fluences of $1.3\times10^{12}$ ions/cm$^2$, and exhibit permanent damage on the barrier, shown as the normal resistance change in Figure 2.13 (b). The mechanism of the irradiation and change of electrical properties were not stated in paper.

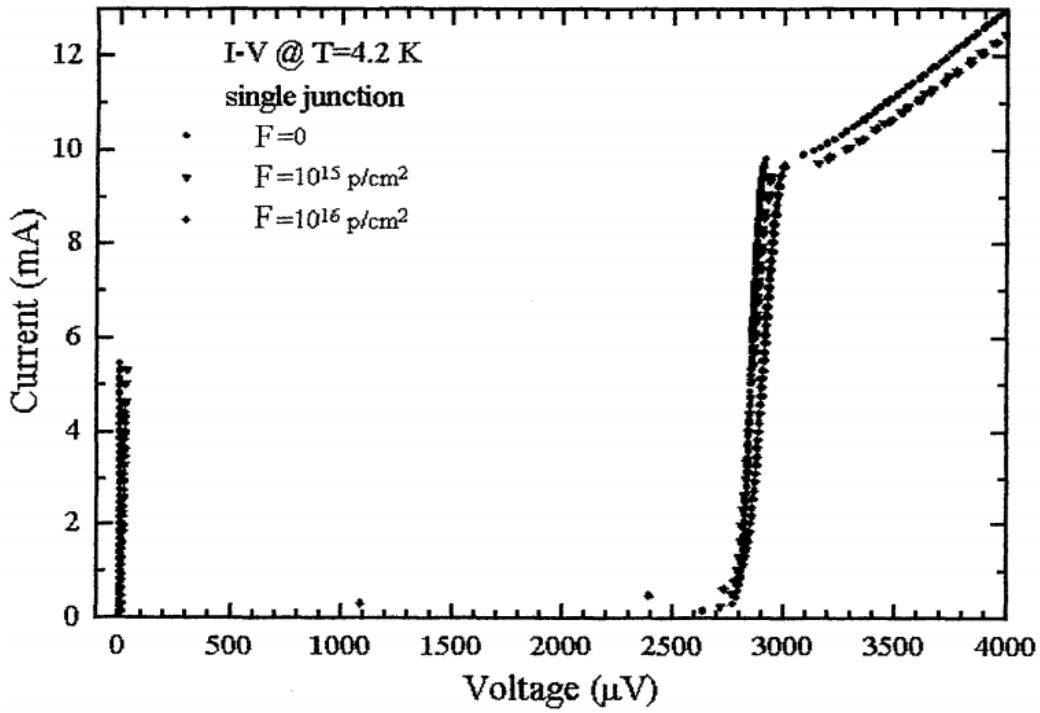


(a)

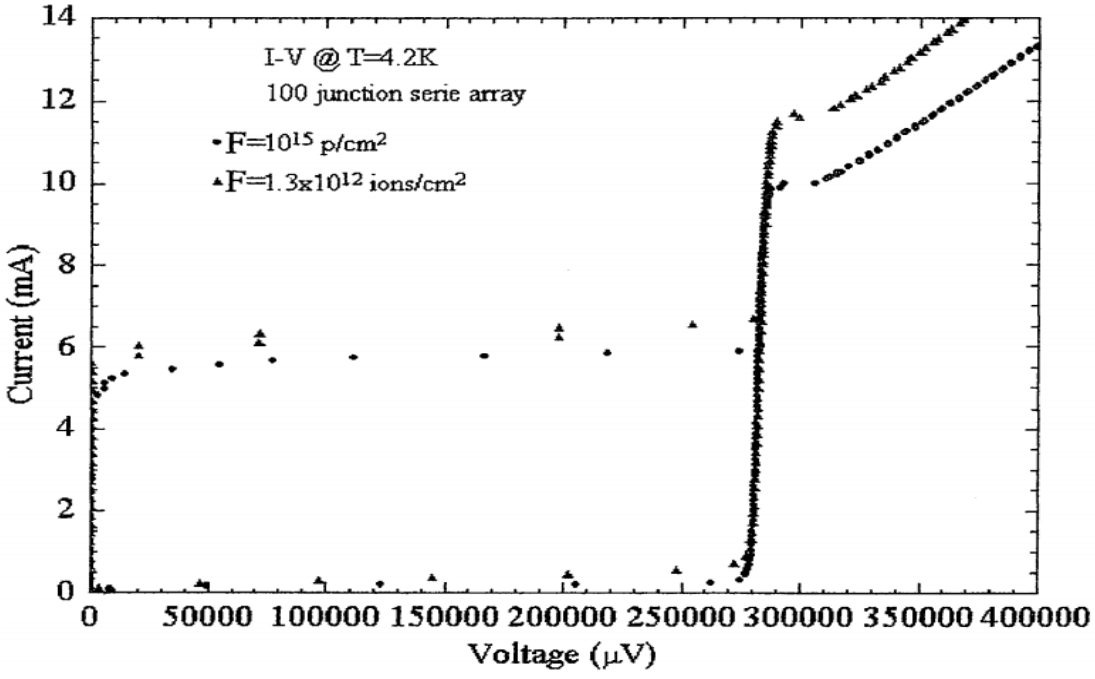


(b)

Figure 2.13 IV characteristic at 4.2K of tunnel junctions before and after (a) $10^{16}$ protons/cm$^2$ irradiation, and (b) $1.3\times10^{12}$ ions/cm$^2$ irradiation. [10]

In Ref [11], 6.5 MeV protons with fluences up to $10^{15}$ protons/cm$^2$ were used to irradiate Nb/Al/AlOx/Nb junctions, as shown in Figure 2.14. One sample was progressively irradiated and characterized at each step, while another sample was directly characterized after a single irradiation at the maximum fluence. Since a change in the energy gap was found only in the first sample, the author concluded that the energy gap change was caused by thermal cycle rather than irradiation damage. However, the author did not investigate the influence of thermal cycling alone on the electrical properties and just assumed that their junctions were not thermally stable.

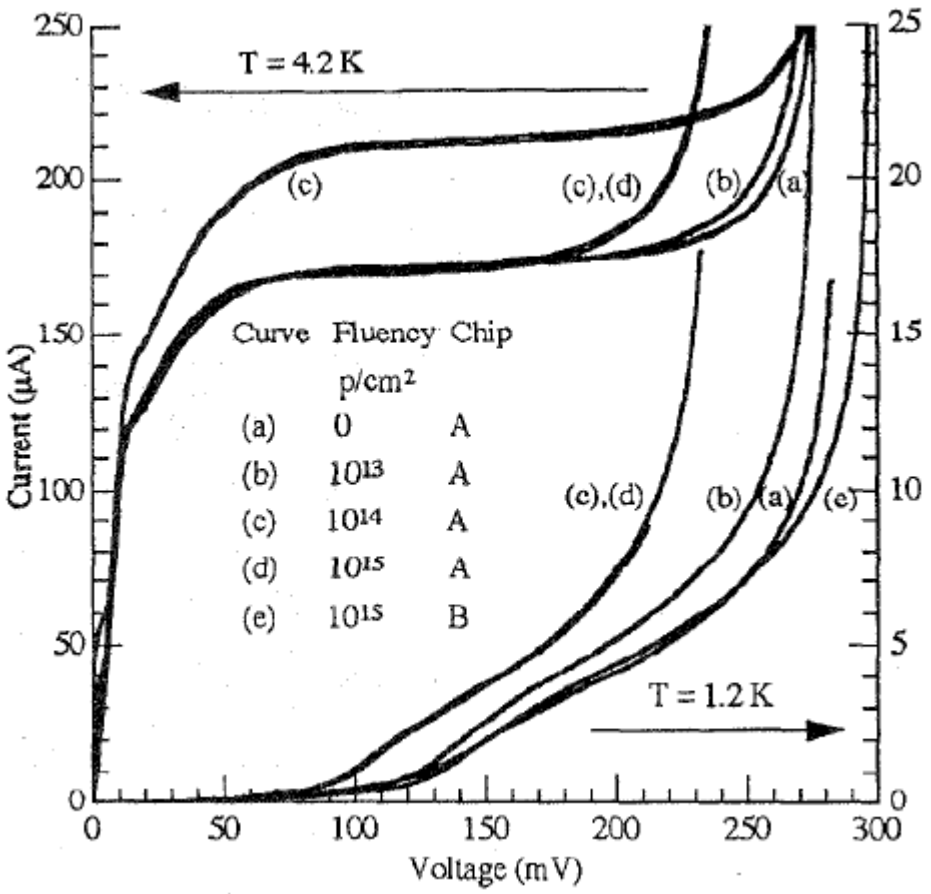


Figure 2.14 IV characteristics of junctions with increasing fluences (chip A) and at maximum fluence only (chip B), measured at 1.2K (lower curves) and 4.2K (upper curves). [11]

In this project, we study the influence of irradiation on the structural, chemical and electrical properties of Nb/Al/AlOx/Nb based Josephson junctions. We will investigate the effects of a wide range of doses on the Josephson junction properties. Also, we will only use Josephson junctions whose electrical properties are stable to thermal cycling. We will take care to establish that this condition is true for both as-made

and irradiated junctions. Our study will also simulate the point defect concentration and amount of intermixing for our study and for those of earlier researchers so that the results can be quantitatively compared and understood.

# CHAPTER 3 EXPERIMENT

## 3.1 Design

In this section, the experimental methodology will be described.

The experiments include the following steps:

1) Fabricate thermally stable Nb/Al/AlOx/Nb Josephson junctions and test the thermal cycle effects on junctions.
2) Irradiate with high energy Helium ion particles, and test the electrical features of junctions after irradiation.
3) Use TEM structural characterization and SRIM modeling simulation to find out the fine details on microscopic level.

## 3.2 Experiment Techniques

### 3.2.1 Device Fabrication

The samples were fabricated at STAR Cryoelectronics LLC at Sante Fe, NM. Films are grown on Si substrates by sputtering process. Nb film is grown in 1900W/0.95mTorr Ar environment, Al film is grown in 300W/0.95mTorr Ar environment. Al is oxidized in 75mTorr Oxygen for 54 minutes. The thickness is shown in the table below.

| Layer | Material | Thickness |
|---|---|---|
| Wiring | Nb | 300nm |
| Insulation | SiO2 | 300nm |
| Top Electrode | Nb | 60nm |
| Barrier | AlOx | 20A |
| Proximity layer | Al | 85A |
| Base Electrode | Nb | 240nm |

Table 3.1 Layer structure of Josephson junction.

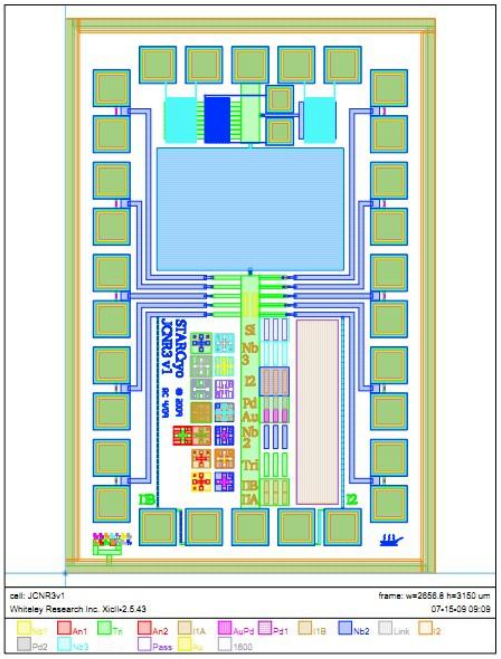

(a)

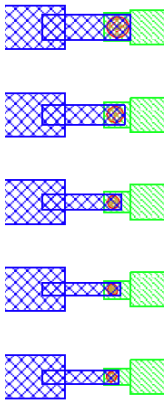

(b)

Figure 3.1 Schematic pin out of the Josephson junction chip. The five junctions on the left side of (a) are unshunted and have the diameters of 10um, 7um, 5um, 4um and 3.5um, respectively from top to bottom, as shown in (b).

### 3.2.2 Wire Bonding

To make electrical measurements, the junction was enclosed in a chip holder that is compatible with our existing cryogenic measurement system. First, the chip was mechanically fastened to a 44 pin chip carrier with photo resist. Then the junction contact pads were connected to the electrical connection pins on a 44-pin chip carrier with 31 microns diameter gold wire. To avoid any damage due to electrostatic discharge, during all these procedures, the wire bonding station is grounded, so the chip carrier is grounded. People should be grounded all the time too, so the sample is grounded when touched by

the gold wire which is held by grounded people. After wire bonding, the samples were kept in anti-static boxes.

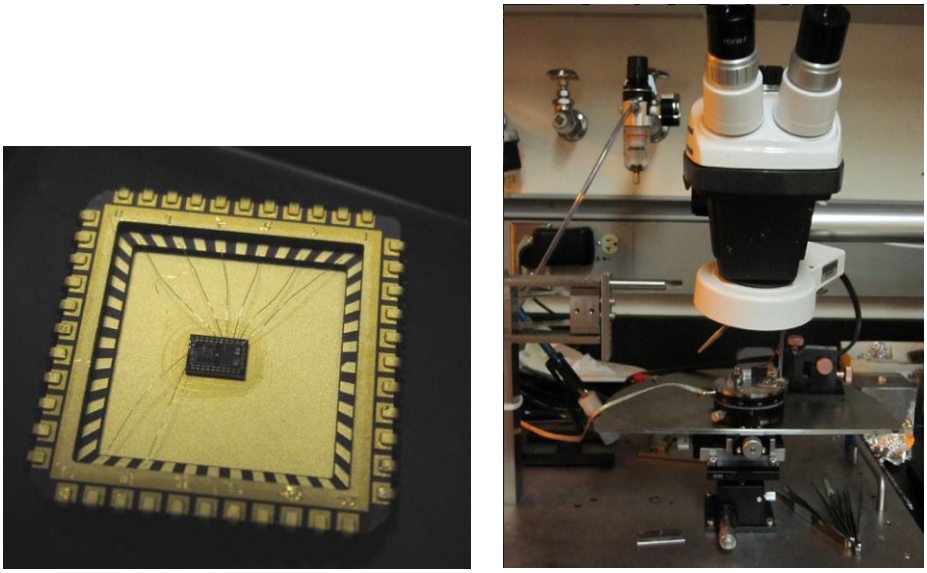

(a) (b)

Figure 3.2 Wire bonded sample and Wire bonding station in the lab.

### 3.2.3 Irradiation

A tandem ion accelerator designed for Rutherford Backscattering Spectrometer was used to introduce defects and intermixing in the layers of the junctions. The irradiation process was carried out at room temperature, in high vacuum ($10^{-7}$ Torr). The alpha particle energy was set at 2 MeV.

The total count of helium ions on the sample is given by:

$$\text{Counts} = \text{Dose}\left(\frac{\text{ions}}{\text{cm}^2}\right) \times \text{Area}(\text{cm}^2) \times \text{ion charge}\left(\frac{\text{coulomb}}{\text{ion}}\right)$$
$$\times \text{chopping factor} \times \text{proportionality constant}\left(\frac{\text{count}}{\text{coulomb}}\right)$$

1 million counts on the detector for a 3mm×3mm spot size correspond to a dose of $3.5\times10^{15}$ ions/cm$^2$. In this paper, the fluence we used was increased from 0 to $5.2 \times 10^{16}$ ions/cm$^2$ in several installments.

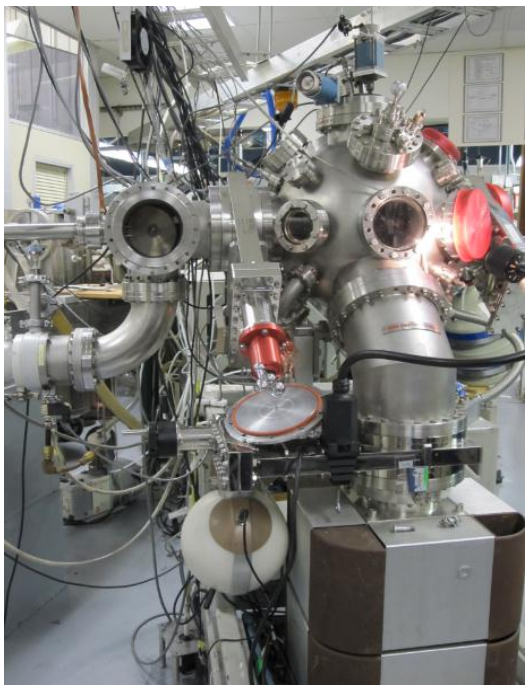

Figure 3.3 Picture of RBS system in the lab.

### 3.2.3 Electrical Measurement

A Faraday shielded room was used when measuring the electrical properties to minimize the influence of noise from the external environment. To avoid damage due to electrostatic discharge, the

relative humidity in the shielded room was maintained above 40%, and antistatic floor mats and grounding wrist straps were used while handling the samples. To minimize ground loops, the shielded room has only one common ground. The measurement system used to characterize all the samples was a commercial analogue unit designed to characterize Josephson Junctions and Superconducting Quantum Intereference Devices (SQUIDs) (Mr. SQUID version 6.4, from STAR Cryoelectronics LLC at Sante Fe, NM), as shown in Figure 3.4. The Mr. SQUID system has an analog to digital attachment to enable computer-controlled data acquisition. We reconfigured the system to be powered by a DC battery in lieu of wall plug power to minimize noise. Four point measurements were performed using BNC cables for the 4 leads, V-, V+, I- , and I+.

A PPMS (Physical Properties Measurement System), as shown in Figure 3.5, was used to enable magnetic field dependent measurements down to cryogenic temperatures. Since PPMS system is too big to fit the shielded room, and the PPMS generate lots of noise itself, it is located outside shielded room. Because of the relatively large noise, it is used only in the magnetic field dependent measurements. In all the other

measurements, samples were placed in a long dipping probe which was inserted a Liquid Helium dewar in the shielded room, shown in Figure 3.6.


Figure 3.4 Front panel of Mr. Squid box


Figure 3.5 Picture of PPMS system in the lab


Figure 3.6 Picture of low temperature measurement system in the lab.

### 3.2.4 Microscopic Characterization

Transmission electron microscopy (TEM) was used for structural and chemical characterization with atomic resolution.

(a)

(b)

Figure 3.7 Picture of TEM system in the lab. (a)ARM200F TEM/STEM station. (b)2010F TEM/STEM station.

### 3.2.5 SRIM Simulation

To detect the fine details at the interface of layers and the percentage of elemental intermixing in junctions, SRIM (the Stopping and Range of Ions in Matter) software program package was used to simulate the irradiation process. It was developed by James Ziegler [35] in 1980s, and has proven to be able to accurately model the concentration and locations of defect generated by particle irradiation. However, SRIM simulates the composition immediately after damage, but cannot accurately predict the annihilation of defects through recombination of vacancies and interstitials. Also, SRIM could not consider the crystallography of samples, so the simulation result is not as accurate as actual experiment.

# CHAPTER 4 RESULTS

## 4.1 Establish Thermally Stable Junctions

To insure that the changes in the electrical characteristics are from the effect of irradiation and not from the measurement process or temporal aging, the Josephson junction was cycled from room temperature (300K) to liquid Helium temperature (4.2K) 10 times. The IV characteristics were measured for each iteration at 4.2K and 300K in un-irradiated and irradiated samples and the results are shown below in Figure 4.1 (a). No significant change in the quasi-particle characteristics was observed, indicating that the junctions are stable against thermal cycling. The zero-voltage current changed from cycle to cycle due to differing levels of flux trapping in the junctions. Then, this junction was irradiated with 15 million counts 2MeV He ion particles, and was cycled 10 times from room temperature to liquid Helium temperature again. The IV characteristics of this junction was measured after 10th dip and shown in Figure 4.1 (b). No change happens either after these thermal cycles.

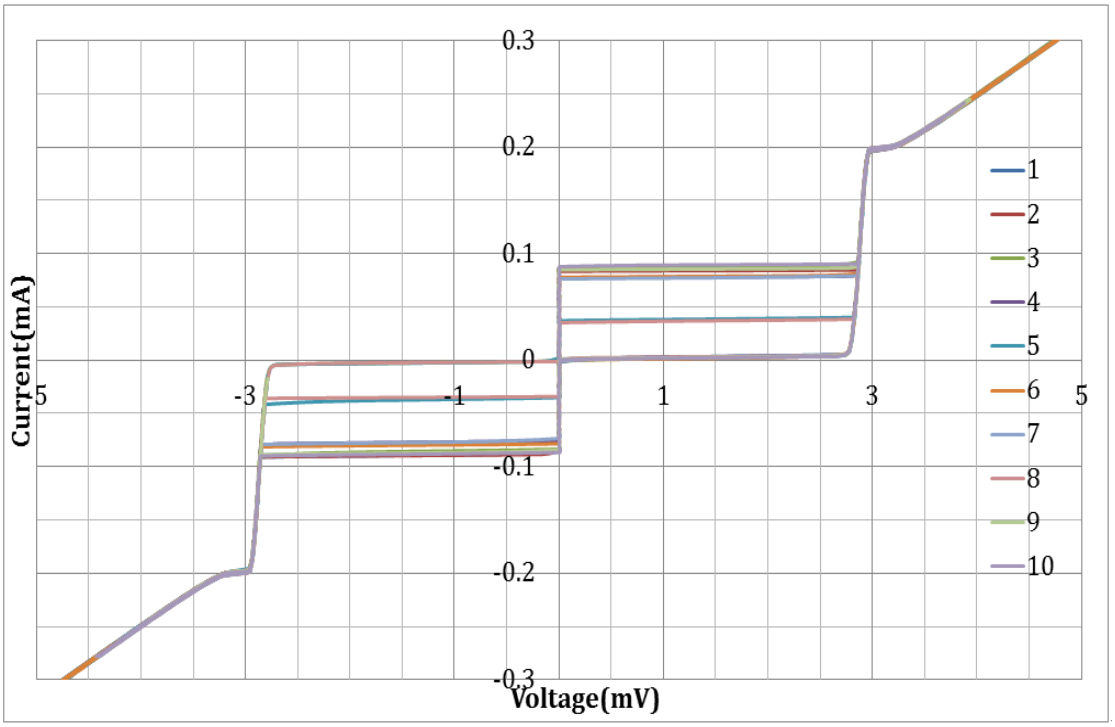


(a)

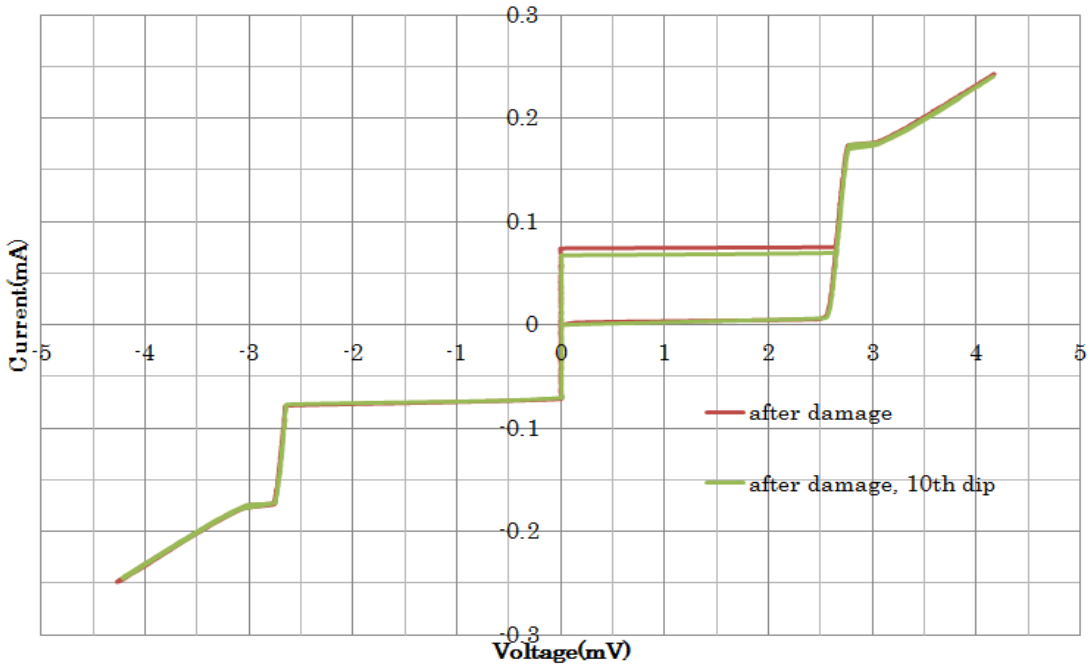


(b)

Figure 4.1 IV characteristic measured at 4.2K each time before and after 10 thermal cycles. (a) Unirradiated junction, (b) Irradiated with 15 million damage junction.

## 4.2 Irradiation Dependence of Josephson Junction Characteristics

Two junctions were irradiated to a maximum fluence of 15 million counts. The first three irradiations were 1 million counts each, the following three irradiations were 2 million counts, and the last one was 6 million counts. Junction #1 was a 38.5 $\mu m^2$ Nb/Al/AlOx/Nb Josephson junction; the IV characteristics after each irradiation are shown in Figure 4.2 (a), in which the energy gap reduces step by step from 2.86mV to 2.73mV (determined by the voltage value at the halfway of gap rising on both positive and negative sides). The rest of the features including the $R_n$, the bound-state knee and supgap currents, are largely unchanged. To make it easier to observe when the changes are found, only the IV curves measured at 4.2K before irradiation, after 9 million counts irradiation, and after 15 million counts irradiation are shown in Figure 4.2 (b). The irradiation-induced changes in the I-V characteristics are mostly observed up to 8 million counts, while there is only a small change in the characteristics after 9 million counts. The onset of subgap current and the knee are rounded off with irradiation, as shown in Figure 4.2 (c) and (d).

Junction #2 is a 78.5μm$^2$ Nb/Al/AlOx/Nb Josephson junction; the IV characteristics after each irradiation were shown in Figure 4.3. The energy gap reduces gradually from 2.78mV to 2.71mV, while the other features are not significantly altered. The onset of subgap current and knee are rounded off with irradiation. This junction is double the junction size of junction #1 and this is reflected in the smaller normal resistance. Other than this difference, the characteristics are essentially identical to that of junction #1.

Junction #3 is a 78.5μm$^2$ Nb/Al/AlOx/Nb Josephson junction; it was irradiated directly to the maximum fluence of 15 million counts. The IV characteristics before and after irradiation are shown in Figure 4.4. The energy gap was reduced from 2.87mV to 2.69mV, while the other features are barely changed. In this figure, the onset of subgap current and knee did not round off, which is a significant difference with the former two junctions.

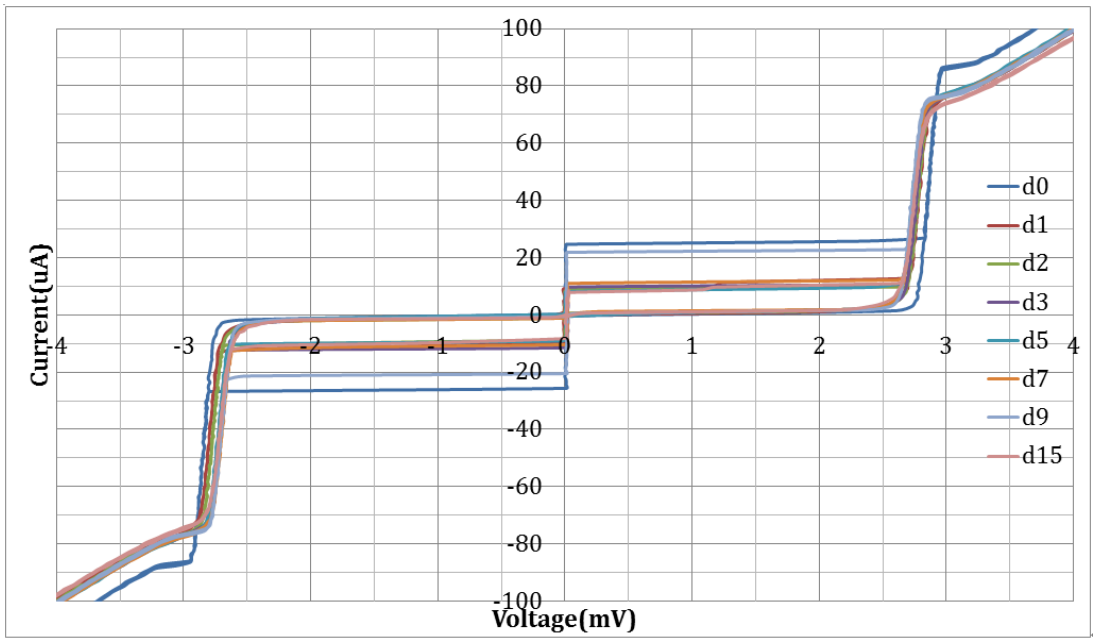
100
80
60
40
20
0
-20
-40
-60
-80
-100
-4
-3
-2
-1
0
1
2
3
4
Current(uA)
Voltage(mV)
d0
d1
d2
d3
d5
d7
d9
d15

(a)

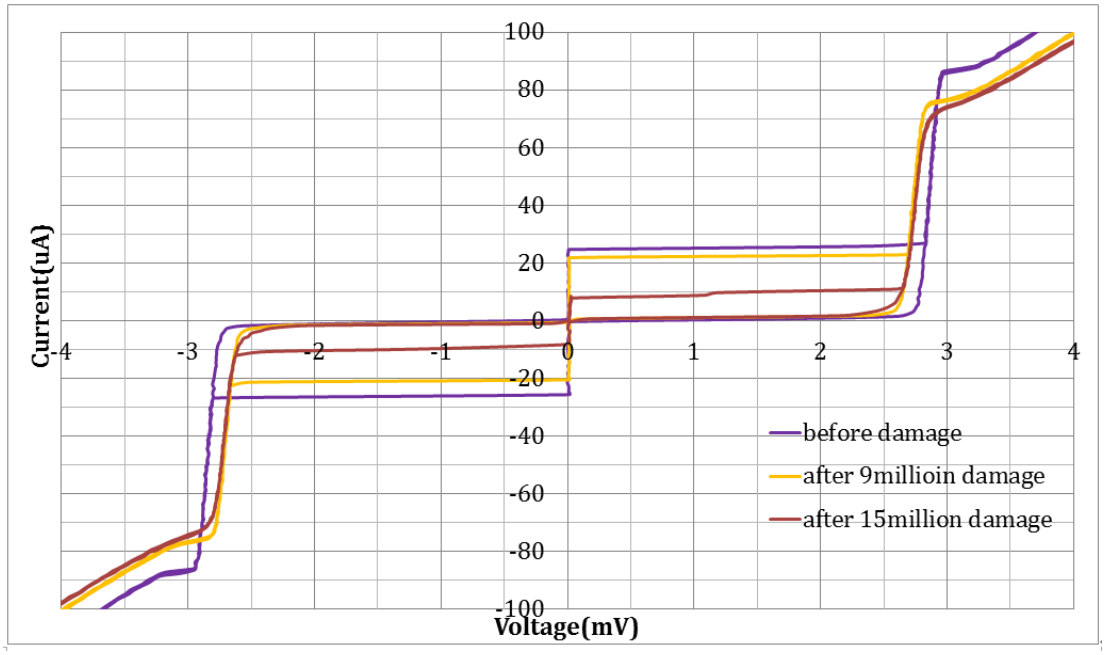
100
80
60
40
20
0
-20
-40
-60
-80
-100
-4
-3
-2
-1
0
1
2
3
4
Current(uA)
Voltage(mV)
before damage
after 9millioin damage
after 15million damage

(b)

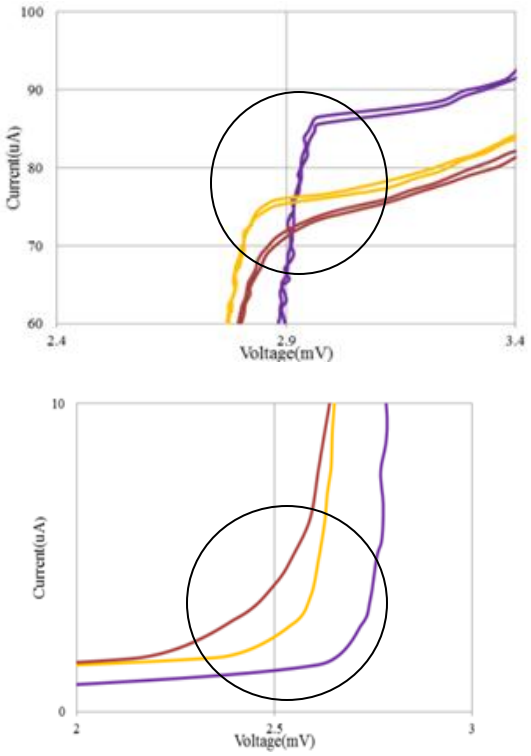


(c) (d)

Figure 4.2 IV characteristics of junction#1. (a) Curves measured at 4.2K after each irradiation. (b) Curves measured at 4.2K before irradiation, after 9million irradiation, and after 15 million counts irradiation. (c) “Knee” of Josephson junction IV feature. (d) Onset of subgap current of Josephson junction IV features.

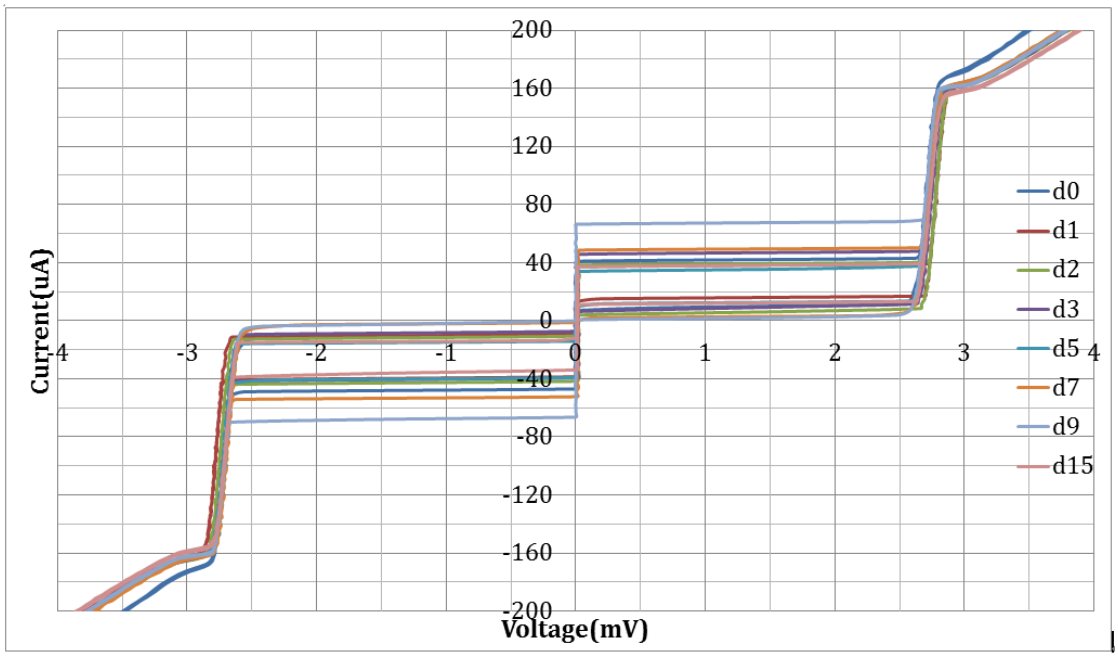


Figure 4.3 IV characteristics of junction#2, measured at 4.2K after each irradiation.

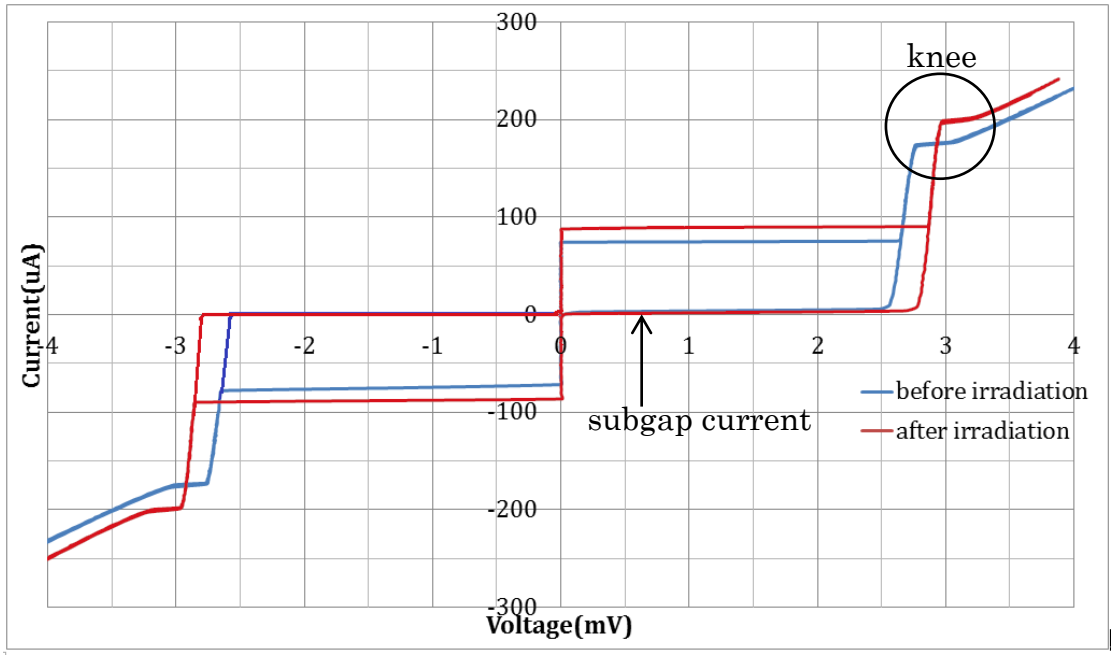


Figure 4.4 IV characteristics of junction#3, measured at 4.2K before and after irradiation.

The energy gap of Nb and the normal resistance of junction are plotted as a function of irradiation dosage in Figure 4.5 and Figure 4.6. The trend observed for the three junctions is similar. For junction #1 and #2, the energy gaps are found to significantly change after each of the first five irradiations, and then only small changes are observed. This reduction is particular evident after the first irradiation. The decrease in the measured gap is a result of the drop in the order parameter in the superconductor layer Nb within a few coherence lengths of the interface or in the proximity layer Al, or in both, as illustrated in Figure 2.7.

The normal resistances of the three junctions increase slightly (about 20%) after the first irradiation and then remain constant for higher doses. This suggests that the tunnel barrier $AlO_x$ is altered slightly after the first irradiation, and is surprisingly largely unaffected by the subsequent irradiation.

The rounding off of the knee, as shown in Figure 4.2 (c), suggests that the disappearance of bound state as a result of changes in the structural or electrical properties of the proximity layer.

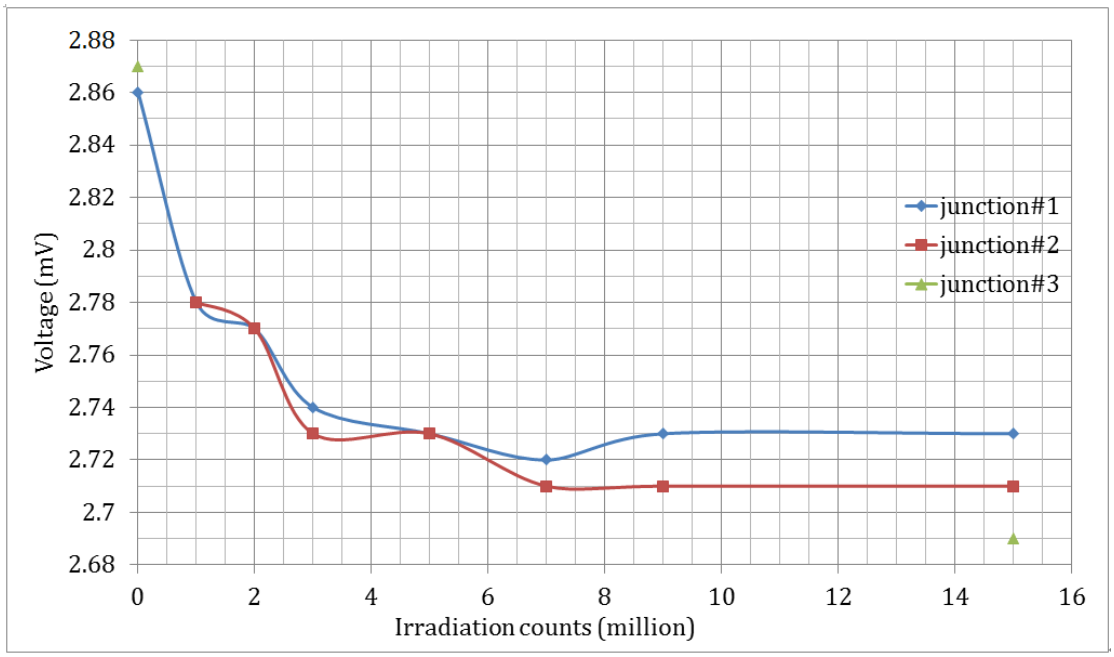


Figure 4.5 Energy gap (2Δ) is plotted against irradiation counts at 4.2K.

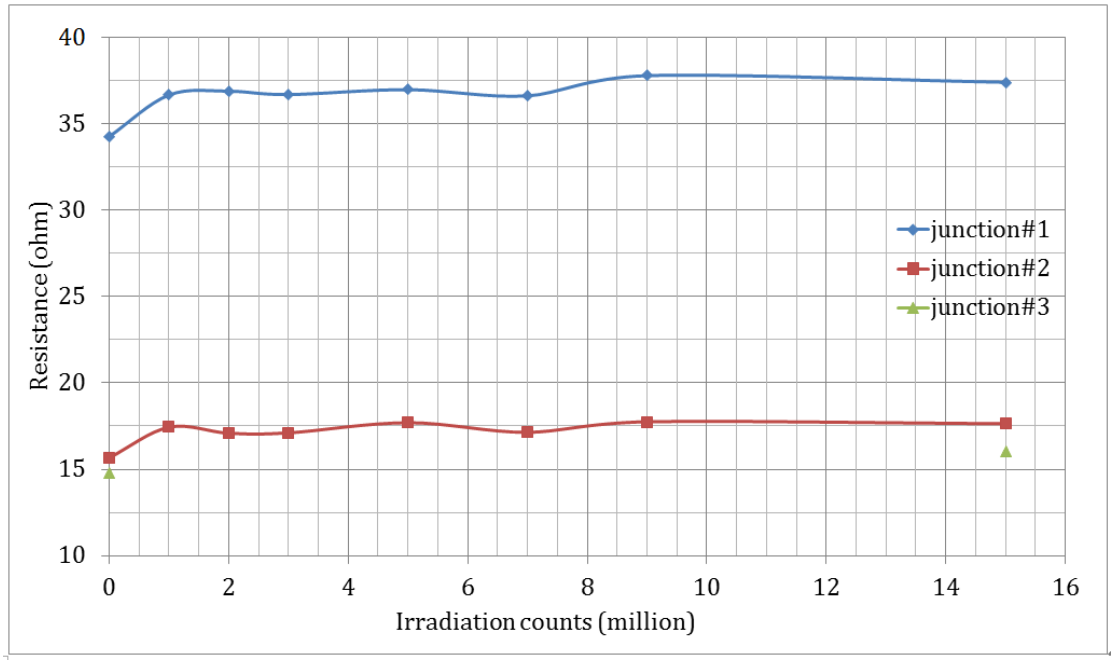


Figure 4.6 Normal Resistance (Rn) is plotted against irradiation counts at 4.2K.

4.3 Temperature dependence

The temperature dependence of undamaged and irradiated Josephson junctions is shown in Figure 4.7. Both curves can be reasonably accurately fit to the theory of Ambegaokar and Baratoff, as discussed in Chapter 2.5.2. The onset of the critical current is reduced from 9.2K to 9.0K. This indicates that the order parameter has decreased by 17 μV (~2%) right at the Nb electrode/barrier interface.

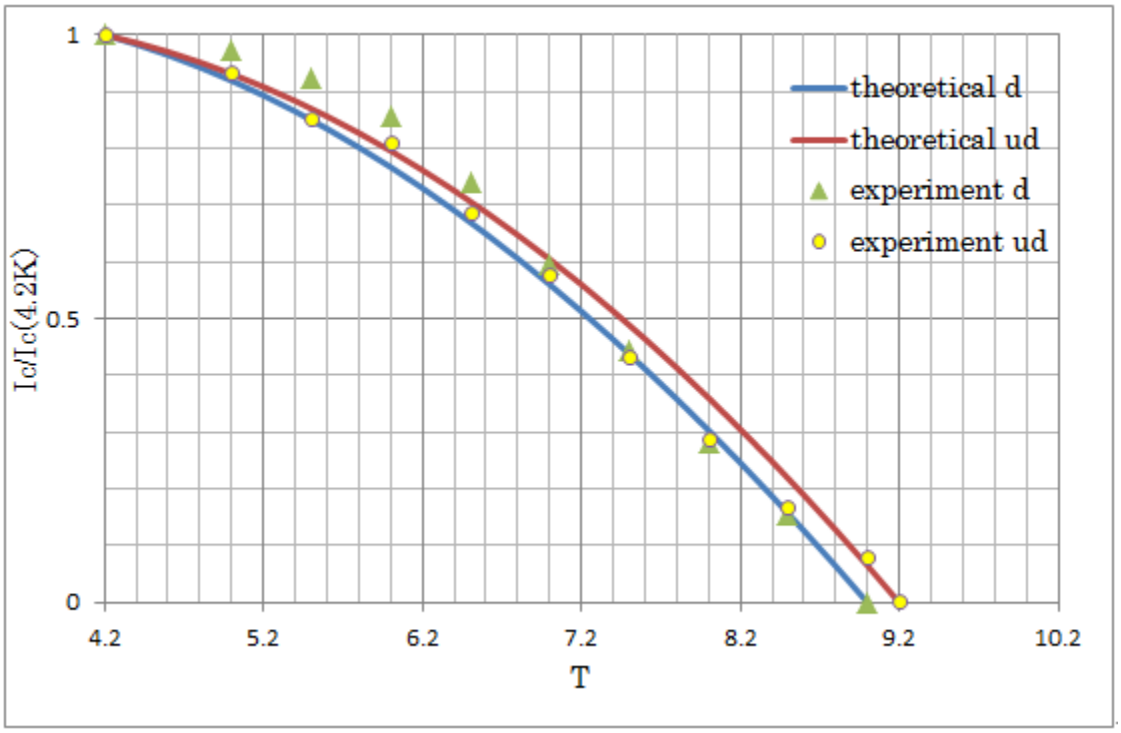


Figure 4.7 Temperature dependence of Josephson current for 15 million counts damaged junction, undamaged junction, and theoretical values.

## 4.4 Magnetic dependence

A magnetic field perpendicular to the junction current could modulate the critical current [21]. Radiation induced structural fluctuations of the barrier properties (energy height and physical depth) would result in a characteristic change in the Fraunhofer pattern.

The magnetic field dependence of the Josephson current of un-irradiated junction (blue dots) and irradiated junction (red dots) is shown in Figure 4.8. The patterns of both curves, including the magnetic field period and the shape of curve, are in accordance with theoretical plot (yellow curve), as discussed in Chapter 2.5.3. The feature does not change after irradiation, suggesting that the intermixing into the Nb electrode is less than the penetration depth.

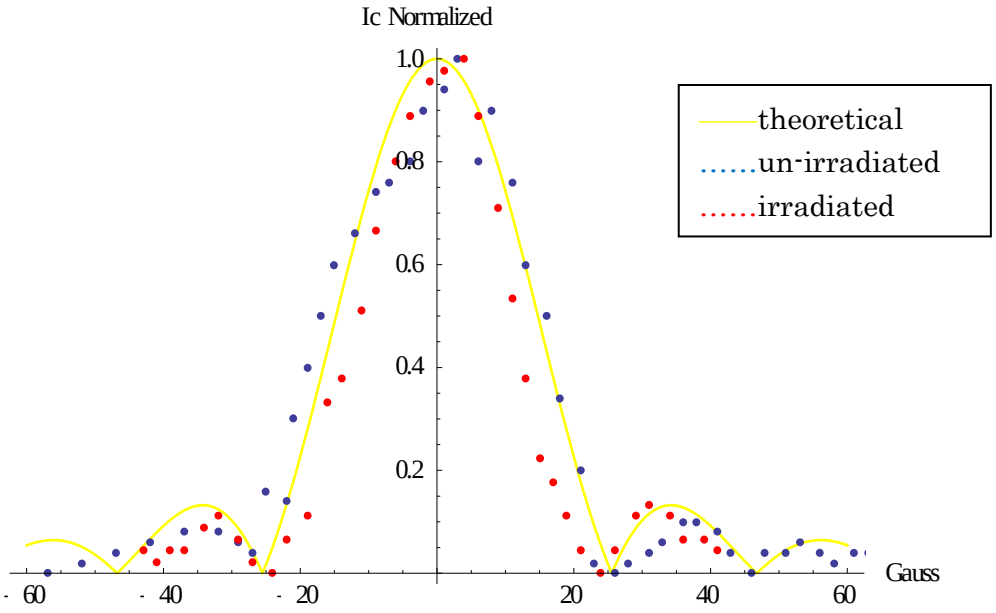


Figure 4.8 Magnetic field dependence of Josephson current before and after exposure to 15 million counts. Also illustration as the solid line is the fit to the theoretical Frahnhofer pattern.

## 4.5 TEM scan

Structural and chemical characterization of the tri-layers was done by examining the sample cross-section under atomic resolution TEM.

The results are shown in Figure 4.9. The interface between top Nb electrode and barrier $AlO_x$, which can be described as the Nb concentration steep drop at 2nm on x-axis in Figure 4.9(a), was clear before irradiation. After irradiation, this interface was intermixed, shown as the Nb concentration gradually drops from 2nm to 6nm on x-axis in Figure 4.9(b). This suggests that the Nb atoms were knocked into $AlO_x$ for about 4nm. Also, the interface between bottom Nb and the proximity layer Al was clear too, shown as the Nb concentration drop from 12nm to 10nm on x-axis in Figure 4.9(a), and turns out to be intermixed after irradiation from 16nm to 10nm on x-axis in Figure 4.9(b). This suggests that the Nb atoms were knocked back into the Al layer for about 4nm. The Al concentration in top Nb electrode did not change, but it increased in bottom Nb electrode for about 30%, which means the Al atoms were knocked into bottom Nb layer during irradiation.


(a)

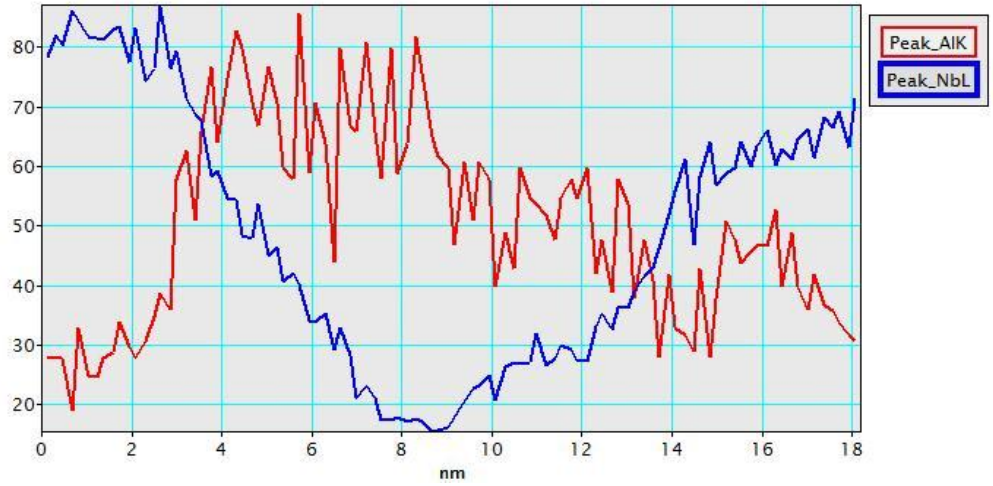


(b)

Figure 4.9 EDX results of (a) undamaged junction and (b) 15 million counts damaged junction.

## 4.6 Simulation

To detect the fine details at the interface of layers and the percentage of element intermixing in junctions, SRIM was used to simulate the atomic displacements during irradiation process. Since the atomic concentration did not change much in SRIM after 5 million counts irradiation, and the electrical measurement result did not change much after 5 million counts irradiation, only 6 million counts irradiation was simulated.

The atom distribution after 6 million counts irradiation was shown in Figure 4.10. Al and O atoms were knocked back into top Nb layer for over 4nm, and into bottom Nb layer for about 6nm. O atoms were distributed all the way into Al layer. The bottom and top Nb atoms were distributed all the way into AlOx barrier and proximity layer Al.

The atomic concentrations of Al, O and Nb in each layer at the interfaces are shown in Figure 4.11. Since the resistivity of AlOx is equivalent to insulator when O concentration is higher than 30%, we define it as barrier when the O concentration is higher than 30%. In this way, the interface between barrier and top Nb moved down for 4nm, and the interface between barrier and proximity layer Al moved down

for 4nm, which makes the barrier thickness unchanged and explains the why $R_n$ in electrical measurements did not change much. Interstitial O decreases Tc by 0.93°K per at.%; while increasing the resistivity in the normal state by 5.2 μΩ cm per at.% [33]. In this way, the intermixing of O in Nb at the barrier interfaces would lead to a drop in order parameter and $T_c$. The intermixing of O and Nb in Al proximity layer leads to a reduced mean free path in Al. This explains and the drop of energy gap, defined by the order parameter within a few coherence lengths of barrier interface.

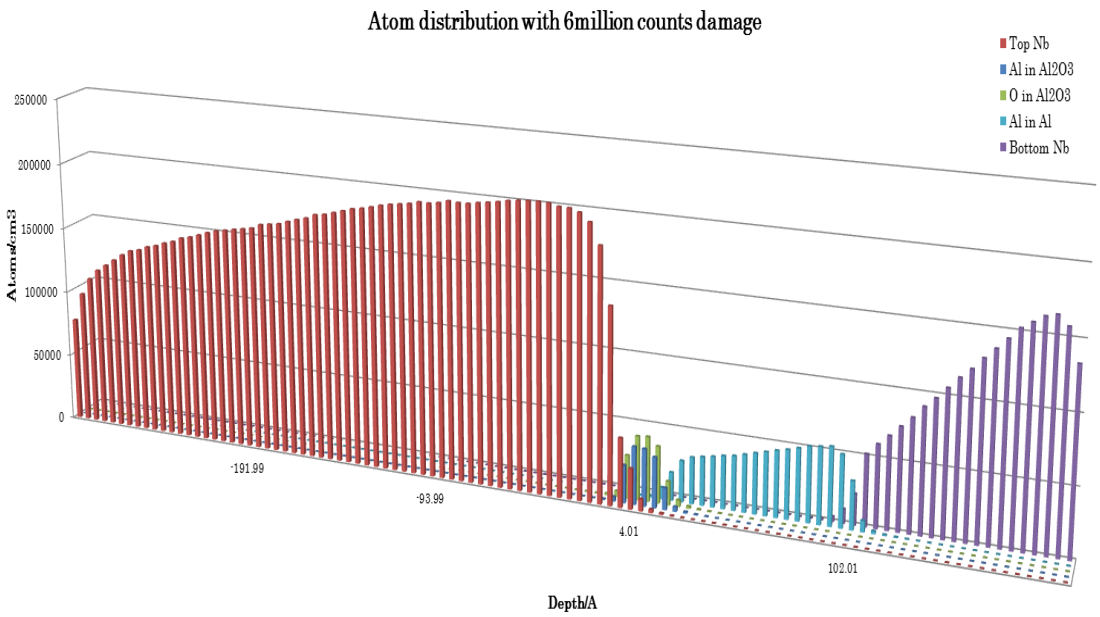


(a)

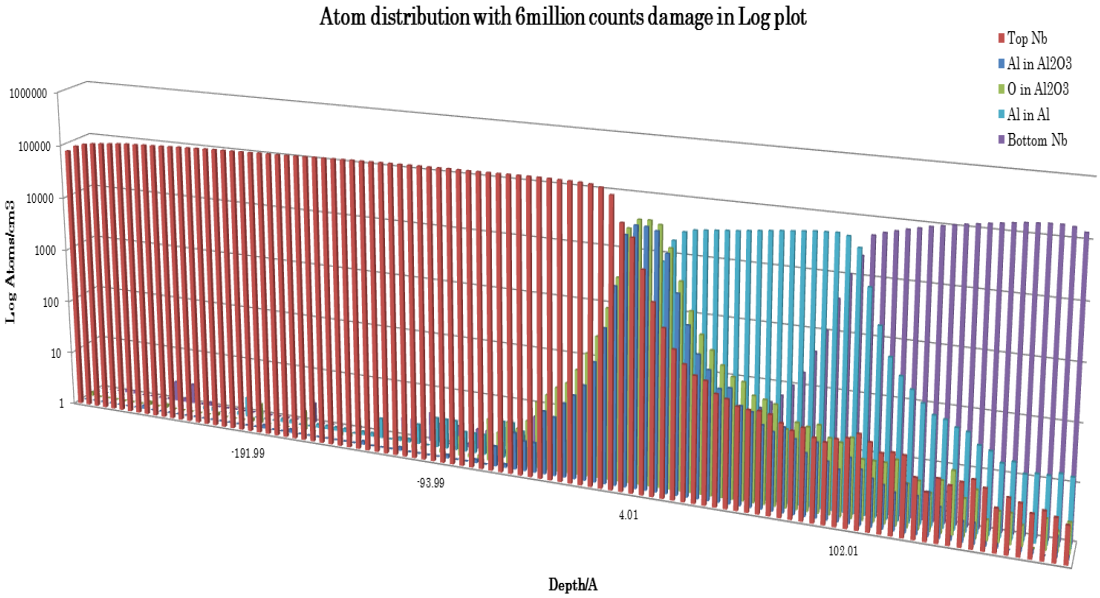


(b)

Figure 4.10 Atom distributions from SRIM simulation of 15 million counts irradiated junction.

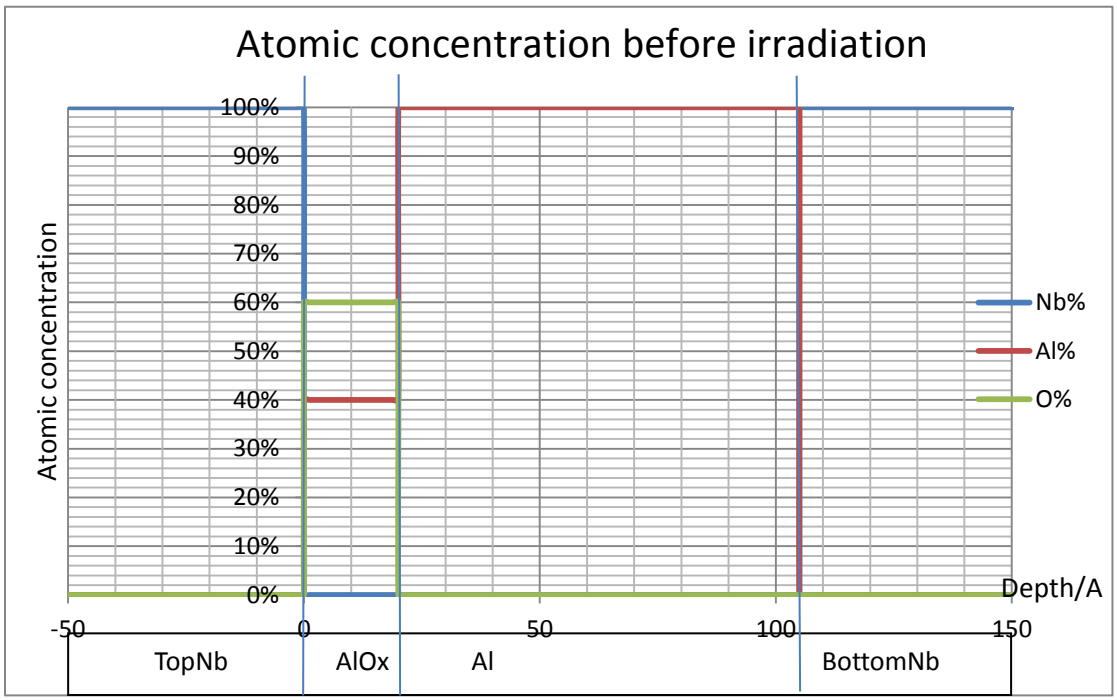


(a)

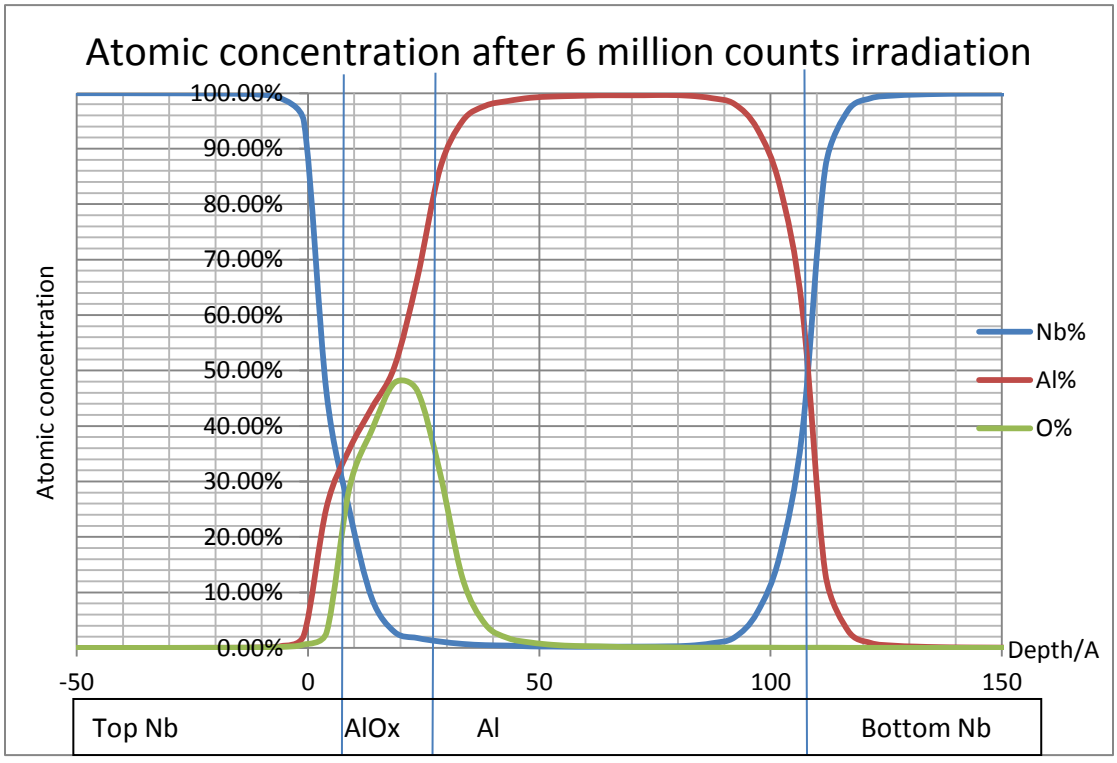


(b)

Figure 4.11 Atom concentration from SRIM simulation of (a) un-irradiated junction and (b) 6 million counts irradiated junction.

## 4.7 Calculation

From the electrical measurement, there is a drop in energy gap. There are two possibilities where the drop occurred. One is from the Al-Nb interface due to proximity effect; another one is from the Al-$AlO_x$ interface due to the diffusion of oxygen from $AlO_x$ into Al.

First we look at the proximity effect at Al-Nb interface. To simplify the intermix problem, we treat the intermixed layer as if it is entirely Al. So we can just look at the change in $T_c$ as the Al layer gets thicker, which is easily modeled by the conventional proximity effect theory, by solving three equations, which have been discussed in Chapter 2.4.

$$\chi(\xi_i^2 k_s^2) = \ln\left(\frac{T_{cs}}{T_c}\right)$$

$$\chi(-\xi_i^2 k_s^2) = \ln\left(\frac{T_{cn}}{T_c}\right)$$

$$\frac{k_s}{k_n}\frac{\rho_n}{\rho_s}\tan(k_s d_s) = \tanh(k_n d_n)$$

According to the detail of the experiment that given me, the known parameters are $T_c$(Nb)=9.2K, $T_c$(Al)=1.7K, Nb thickness=2500A, Nb coherence=100 A (the values are spread between 27A to 270A from the literature), rr=the resistivity ratio between Al and Nb. Since rr is not very well known to us at this moment, $T_c$ was calculated as function of Al thickness for a range of rr values.

For the Nb we have in the junction which are grown under RT, the resistivity should be around 10-20μΩ·cm at 9K. For clean Al the resistivity at 9K should be much smaller than 1μΩ·cm. Dirty Al with 5%-10% Oxygen has resistivity 10μΩ·cm at 9K. It seems we have rr much less than 1 before damage occur. The damage process effectively adds a dirty Al layer so rr eventually becomes close to 1. In all case of rr values the proximity effect between Al-Nb will lower $T_c$ no more than 0.08K. We can pretty much exclude the possibility that proximity effect of extra Al and Al-Nb mixed layer can lower the gap we measured.

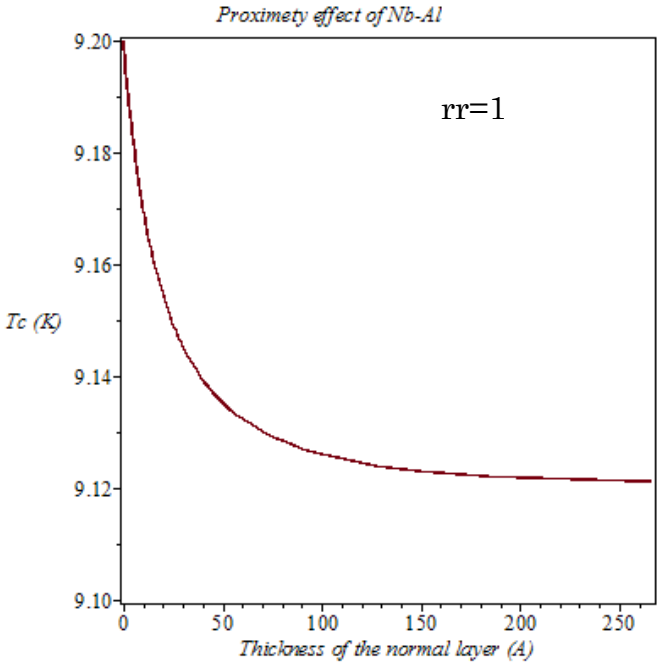


(a)

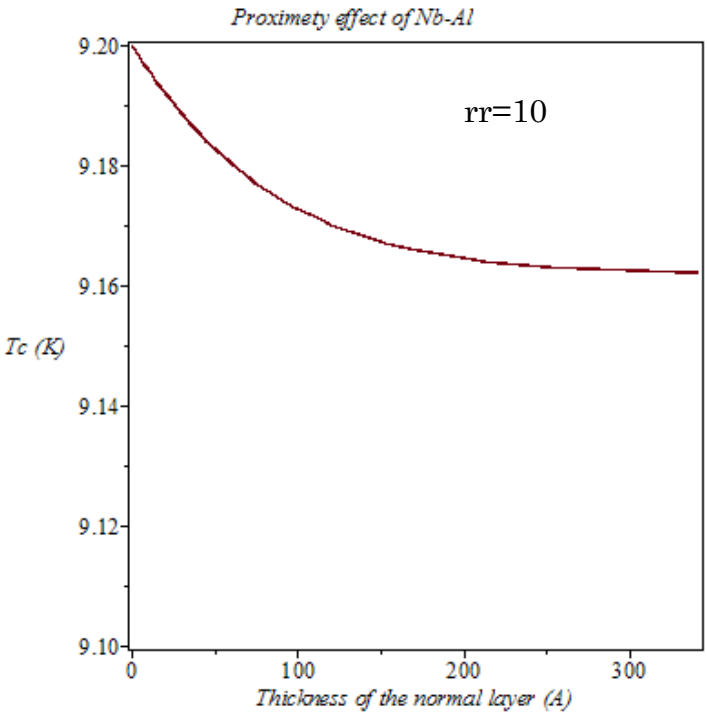


(b)

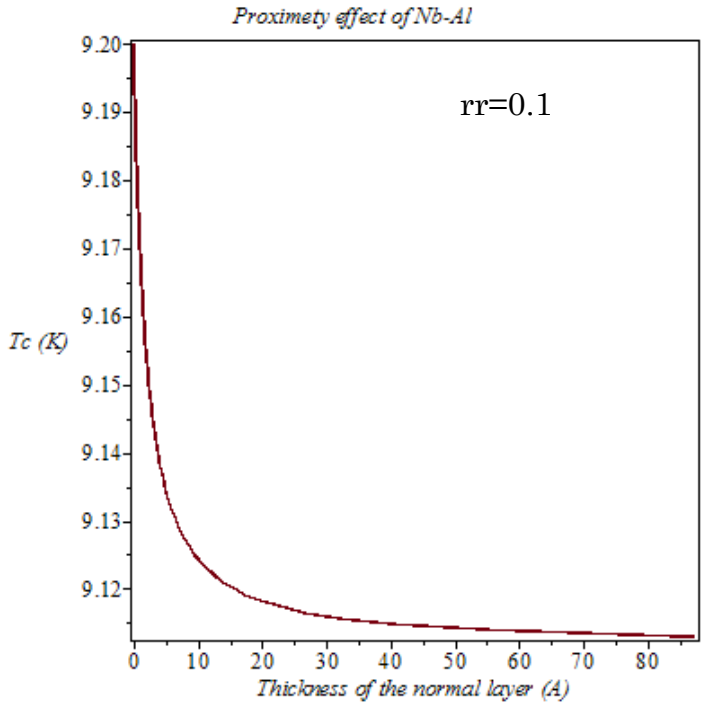


(c)

Figure 4.12 Proximity effect of Nb-Al when the resistivity ratio of Al and Nb is (a) 1; (b) 10; (c) 0.1.

Next let us look at the situation at Al-$AlO_x$ interface. We expect oxygen diffusion from $AlO_x$ to Al, create a layer of slightly oxidized Al between the original $AlO_x$ and Al layer. We have experiment results shows that Al layers have 5% and 7% oxygen has 9K resistivity of 8 and 11μΩ·cm respectively. Based on ion-damage simulation data, I will first model the effect by a uniform Al layer with 20% oxygen and 25A thick. A liner extrapolation with give resistivity of 20% Oxygen at 30μΩ·cm, but the increase rate should be much fast than linear. I used the number of 50μΩ·cm.

The decay of Δ inside normal region is described by the exponential factor $\exp\left(\frac{\delta t}{\xi_n}\right)$ where $\delta t$ is the thickness and $\xi_n = \sqrt{\frac{\hbar v_f l}{k_B T}}$.

After calculation of the two equations, which have been discussed in Chapter 2.4:

$$\xi_{N,S} = \left(\frac{\hbar D_{N,S}}{2\pi k_B T}\right)^{1/2}$$

$$D_{N,S} = \frac{1}{3} v_{F_{N,S}} l_{N,S}$$

the result shows an extra 25A thick 50μΩ·cm layer will cause D drop from 1 to ~0.85, roughly 15%. Similarly an extra 25A thick clean Al

layer will only cause D drop from 1 to ~0.99. This shows a thin oxidize Al layer can decrease the observed gap.

# CHAPTER 5 CONCLUSION

In this work, we studied the influence of 2MeV Helium ion irradiation with doses up to $5.2 \times 10^{16}$ ions/cm$^2$ on the tunneling behavior of Nb/Al/AlOx/Nb Josephson junctions. Structural and analytical TEM characterization, combined with SRIM modeling, indicates that over 4nm of intermixing occurred at the interfaces. EDX analysis after irradiation, suggests that the Al and O compositions from the barrier are collectively distributed together over a few nanometers. Surprisingly, the IV characteristics were largely unchanged. The normal resistance, $R_n$, increased slightly (<20%) after the initial dose of $3.5\times10^{15}$ ions/cm$^2$ and remained constant after that. This suggests that tunnel barrier electrical properties were not affected much, despite the significant changes in the chemical distribution of the barrier's Al and O shown in SRIM modeling and TEM pictures. The onset of quasi-particle current, sum of energy gaps ($2\Delta$), dropped systematically from 2.8meV to 2.6meV with increasing dosage. Similarly, the temperature onset of the Josephson current dropped from 9.2K to 9.0K. This suggests that the order parameter at the barrier interface has

decreased as a result of a reduced mean free path in the Al proximity layer and a reduction in the Nb electrode transition temperature near the barrier. The dependence of Josephson current on the magnetic field and temperature does not change significantly with irradiation; suggesting that intermixing into the Nb electrode is significantly less than the penetration depth.

This study showed that Nb/Al/AlOx/Nb Josephson junctions are very stable with high energy particle irradiation. Their electrical characteristics almost remain unchanged even when the chemical composition at the interfaces is highly influenced by the incident high energy particles. These Josephson junctions are very reliable to be widely used in applications that need exposure to high energy particle irradiation.

# REFERENCES


[1] B. D. Josephson. Possible new effects in superconductive tunneling. Physics Letters 1, 251 (1962).

[2] P. Anderson, J. M. Rowell. Probable Observation of the Josephson Superconducting Tunneling Effect. Physical Review Letters 10 (6): 230 (1963).

[3] J. Clarke, W. M. Goubau and M. B. Ketchen. Tunnel junction dc SQUID: fabrication, operation, and performance. Journal of Low Temperature Physics, 25, 99 (1976).

[4] S. P. Benz and C. A. Hamilton. A pulse-driven programmable Josephson voltage standard. Applied Physics Letters, 68, 3171 (1996).

[5] T. A. Fulton, P. L. Gammel, D. J. Bishop, L. N. Dunkleberger, and G. J. Dolan. Observation of combined Josephson and charging effects in small tunnel junction circuits. Physics Review Letters, 63, 1307–1310 (1989).

[6] K. K. Likharev and V. K. Semenov. RSFQ Logic/Memory Family: A New Josephson junction technology for sub-terahertz-clock-frequency digital systems. IEEE Transactions on Applied Superconductivity, 1, 3 (1991).

[7] J. Zmuidzinas and P. L. Richards. Superconducting detectors and mixers for millimeter and submillimeter astrophysics. Proceedings of the IEEE 92, 1597 (2004).

[8] S. E. King, R. Magno, and W. G. Maisch, Radiation damage assessment of Nb tunnel junction devices, IEEE Transactions on Nuclear Science, Vol. 38, No. 6, pp. 1359-1364 (1991).

[9] I. Péron, G. Faury, Y. Delorme, F. Dauplay, B. Lecomte, M. Salez and K. F. Schuster, Investigation of radiation hardness of SIS junctions for space borne radio astronomy, Journal of Physics IV France, Vol. 12, No. 3, pp. 169-172 (2002).

[10] L. Frunzio, R. Cristiano, and S. Pagano, Radiation hardness of Josephson devices, Japanese Journal of Applied Physics, Vol. 37, Suppl. 2, pp. 40-45 (1998).

[11] S. Pagano, R. Cristiano, L. Frunzio, V. G. Palmieri, G. Pepe, R. Gerbaldo, G. Ghigo, L. Gozzelino, E. Mezzetti, and R. Cherubini, Effect of intense proton irradiation on properties of Josephson devices, IEEE Transactions on Applied Superconductivity, Vol. 7, No. 2, pp. 2917-2920 (1997).

[12] J. M. Rowell, M. Gurvitch, J. Geerk, Modification of tunneling barriers on Nb by a few monolayers of Al. Physical Review B, vol. 24, No. 4, pp. 2278-2281 (1981).

[13] M. Gurvitch M. A. Washington and H. A. Huggins. High quality refractory Josephson tunnel junctions utilizing thin aluminum layers. Applied Physics Letters, vol. 42, No. 5, pp. 472-474 (1983).

[14] H. karmerlingh Onnes, Leiden Comm. 120b, 120b, 124c (1911).

[15] Meissner, W. and R. Bochsenfeld, Ein neuer Effekt bei Eintritt der Supraleitfähigkeit. Naturwissenschaften 21 (44): 787–788 (1933).

[16] <http://en.wikipedia.org/wiki/Meissner_effect>.

[17] J. Bardeen, L. N. Cooper, and J. R. Schrieffer, Theory of Superconductivity, Physics Review, 108, 1175 (1957).

[18] Abrikosov, A. A. On the magnetic properties of superconductors of the second group, Soviet Physics JETP 5, 1174 (1957).

[19] Michael Tinkham, Introduction to Superconductivity, 2nd Edition, McGraw Hill, New York (1996).

[20] F. and H. London, Proceedings of the Royal Society (London), A149, 71 (1935).

[21] Barone and G. Paterno, Physics and Applications of the Josephson Effect, John Wiley & Sons, Inc. (1982).

[22] Kittel, Introduction to Solid State Physics, 5th Edition, John Wiley & Sons, Inc. (1976).

[23] S. Basavaiah, J. M. Eldridge, and J. Matisoo, Tunneling in lead - lead oxide - lead junctions, J. Appl. Phys. **45**, 457 (1974).

[24] Charles P. Poole Jr., Horacio A. Farach, and Richard J. Creswick, Superconductivity, Academic Press, Inc. (1995).

[25] Andreev, A. F. (1964). "Thermal conductivity of the intermediate state of superconductors". Sov. Phys. JETP 19: 1228.

[26] P.G. de Gennes, Boundary Effect in Superconductors, Rev. Mod. Phys., vol. 36, pp. 225-237 (1964).

[27] T Löfwander, V S Shumeiko and G Wendin, Andreev bound states in high Tc superconducting junctions, Superconductor science and Technology, Vol. 14, No. 15, pp. R53-R77 (2001).

[28] N. R. Werthamer, Theory of the superconducting transition temperature and energy gap function of superposed metal films, Physics Review B, Vol. 132, pp. 2440-2445, Jan. (1964).

[29] P. R. Broussard, Boundary condition effect on the superconducting transition temperature of proximity effect system, Physics Review B, Vol. 43, pp. 2783-2787, Feb. (1991).

[30] N. L. Rowell, H. J. T. Smith, Investigation of superconducting proximity effect by Josephson tunneling, Canadian Journal of Physics, 54(3): 223-226, 10.1139/p76-026 (1976).

[31] V. Ambegaokar and A. Baratoff, Tunneling between superconductors, Errantum of Physics Review Letter, Vol. 10, pp. 486-491 (1963).

[32] J. Matisoo, Critical currents and the current distributions in Josephson junctions, Journal of Applied Physics, Vol. 40, No. 4, pp. 1813-1820 (1969).

[33] NCRP, Ionizing radiation exposure of the population of the United States, Report No. 93 (1987).

[34] Cameron Kopas, Chase Yurga-Bell, Thermodynamics of radiation damage in electronic devices, Unpublished (2011).

[35] James Ziegler, SRIM&TRIM, <http://www.srim.org/>.

[36] Warren DeSorbo, Effect of Dissolved Gases on Some Superconducting Properties of Niobium, Phys. Rev. 132, 107–121 (1963).